Improvements for the inverse acoustic characterization of multi-layer porous materials in impedance tube

Rémi Roncen, Zine El Abiddine Fellah, Erick Ogam

Improvements for the inverse acoustic characterization of multi-layer porous materials in impedance tube

R. Roncen *[1], Z.E.A. Fellah[2] and E. Ogam[2]

[1]ONERA /Département Multi-Physique pour l'Énergétique, Université de Toulouse, F-31055, Toulouse, France

[2]Laboratoire de Mécanique et d'Acoustique, Centre National de la Recherche Scientifique, Unité Mixte de Recherche 7031, Aix-Marseille Université, Centrale Marseille, F-13402 Marseille Cedex 20, France

Abstract

The impedance tube is a widespread tool in the acoustic research community and has proven efficient in retrieving the intrinsic properties of some porous materials using an acoustic inverse method. However, these inverse methods can be biased because of the improper consideration of the uncertainty on the signals used for the inference (usually, the surface impedance or reflection coefficient). This bias is highlighted and a straightforward solution is suggested.

A refinement of the statistical Bayesian inference strategy in impedance tubes is then proposed, which can be applied on single layer materials as well as multi-layer materials (three layers maximum are tested). When performing a single acoustic observation on a multi-layer material, the problem can become severely ill-posed, because of the non-uniqueness of the inverse problem solution, and the lack of sensitivity of some parameters. To lift these issues, multiple air-gaps are added between the material and the rigid backing of the impedance tube to artificially increase the number of observations, non-intrusively. Different test cases are considered for three numerically simulated porous materials of different intrinsic properties, assembled in twelve different multi-layer structures to test the robustness of the method on synthetic noisy data. A multiple-try differential evolution sampling is used to tackle the statistical Bayesian inference problem.

Key-words: impedance tube; porous materials; material characterization; Bayesian inference; multi-layer materials

1 Introduction

A porous material can be represented as the combination of a solid phase and a fluid phase. Interactions and energy exchanges occurring between the two phases give rise to the dissipation of waves traveling through the porous medium. In air, wave dissipation is mostly caused by viscous and thermal effects, which strongly depend on the pore microstructure. To represent this geometry at the macroscopic scale, several intrinsic porous material properties have been derived and integrated in models governing the acoustic wave behavior.

*Corresponding author: remi.roncen@onera.fr

These intrinsic properties (i.e., porosity, tortuosity, pore size, etc.) are of interest in a wide range of applications outside the acoustics domain, because porous media are largely present in our environment and are used in various fields : in geophysics [1] for the detection of seismic waves [2, 3] or for the detection of land mines [4, 5]; in medicine for the study of bones [6–8]; in aeroacoustics for the reduction of trailing edge noise [9–11]; in thermal engineering, for transpiration-cooling in combustion chambers [12, 13]; in room acoustics, as sound absorbing foam [14, 15]. A shared feature of these research topics is that the knowledge of the intrinsic properties of porous materials is needed for the use of predictive models (i.e., wave propagation in soil for seismic applications, risk fracture assessment for porous bone, acoustic absorption for foams). A community has developed around the idea that acoustic inverse methods could be used to gain information on the properties of porous media [16–31]. This kind of indirect measurement, coined inference, has proven reliable provided that precise acoustic models could be used. It complements or replaces altogether the difficult task of having to directly measure each property separately.

There seems to be three important choices that one must make before attempting such an inverse method: the frequency content of the signal (low frequency in wave guides [16, 20, 22–25, 27, 28], or high frequency with ultrasonic transducers in free space [16–19, 21, 26, 29–31]), the nature of the inference (deterministic when an optimization approach is used [16–19, 21–23, 25], or statistic when a Bayesian inference is used [20, 25–31]), and the type of signal (time-domain [17–19, 21, 26, 28–30] or frequency-domain [16, 20, 22, 23, 25, 27, 31]). In the present work, only one of the 2^3 possible choice combinations is studied : frequency-domain signals at low frequencies using a Bayesian inference approach. However, one will find that the method can be applied to other types of inference straightforwardly, as will be discussed in Sec. 5.6.

Although the problem of single-layer material identification has been broadly studied, there is very little in the literature about the identification of multi-layer materials with acoustic inverse methods, i.e., finding simultaneously the intrinsic properties of two or more than two materials that are stacked on one another. When dealing with a fixed number of known materials that can be characterized independently, there is no need for such a multi-layer identification. However, when a single material is inhomogeneous and can be approximated by a discrete number of unknown layers, the method becomes relevant.

To the best of our knowledge, only a recent contribution [27] has attempted the analysis of such a problem, using two levels (parameter identification and model selection) of Bayesian inference, showing that it was possible to not only detect the number of layers in a material, but also identify some of their properties. However, as in other studies before [20, 28, 29], ill-posedness is present in the identification, i.e., there is a non-uniqueness, an indetermination of the obtained solution. Bayesian inference methods are well suited for this kind of difficult task, in that they yield posterior probability densities for the parameters of interest, containing all the knowledge one is able to extract from the signals. Thus, the non-uniqueness of the solution can be characterized, provided that the Bayesian inference sufficiently and efficiently explored the parameter space.

This paper sets two goals. The first one is showing that using surface impedance or reflection coefficient obtained from impedance tubes for material inverse characterization is bound to yield biased inference results, because of uncertainties not being correctly taken into account. The second objective is the development of a technique, based on the addition of air-gaps behind the samples, to reduce the ill-posedness and improve the knowledge on material properties of both single- and multi-layer samples. Although air-gaps are traditionally used to improve the acoustic absorption of sound-absorbing foams in the low-frequency range [32], they are used in this work to gain additional observations of the same samples for identification purposes. This was attempted previously in Ref. [33], albeit with additional boundary conditions at the end of the impedance

tube. In this regard, the present study complements the work of Ref [27], adding a straightforward strategy to remove ill-posedness during the inversion.

The paper is organized as follows. The acoustical model and methods applied to a porous material are first recalled in Sec. 2. The source of the biases introduced by the consideration of derived signals in an impedance tube is then presented in Sec. 3. The Bayesian inference framework is developed in Sec. 4.1. Section 5 presents and discusses the identification results obtained on 15 different *numerical* materials with synthetic noisy data, and Sec. 6 summarizes the takeaway messages and concludes the paper.

2 Acoustical model and methods

The porous material samples are assumed to have a rigid structure. Porous samples thus behave as an equivalent fluid when considering the dissipation of an acoustic wave traveling within the intra-pore fluid phase (air). Viscous effects are introduced in the definition of a complex frequency-dependent density $\tilde{\rho}_{\text{eq}}$, whereas thermal effects are introduced in the definition of a complex frequency-dependent bulk modulus $\tilde{K}_{\text{eq}}$. The equation controlling the wave behavior inside the fluid phase is written

$$\Delta p + \omega^2 \frac{\tilde{\rho}_{\text{eq}}}{\tilde{K}_{\text{eq}}} p = 0. \tag{1}$$

The focus here is placed on the identification process, and not on taking the most detailed or complex model of the literature for the pore dissipation. It was chosen to use the Johnson-Champoux-Allard-Pride-Lafarge (JCAPL) model with Horoshenkov hypotheses [34] on the pore distribution for the following investigations, see Sec. 2.1.

2.1 Semi-phenomenological model of Horoshenkov for dissipation within the fluid phase

The dissipation in the pores is accounted for by the JCAPL model [35–38] and the hypotheses on the pore distribution by Horoshenkov [34], i.e., the pore sizes follow a log-normal distribution and the pores have a circular shape. The JCAPL model for viscous dissipation can be written

$$\tilde{\rho}_{\text{eq}} = \frac{\rho_f}{\phi}\tilde{\alpha}(\omega), \quad \tilde{\alpha}(\omega) = \alpha_\infty \left[1 + \frac{1}{\mathrm{j}\bar{\omega}}\tilde{F}(\omega)\right], \tag{2}$$

$$\tilde{F}(\omega) = 1 - P + P\sqrt{1 + \frac{M}{2P^2}\mathrm{j}\bar{\omega}}, \quad \bar{\omega} = \omega\rho_f \frac{k_0\alpha_\infty}{\mu\phi}, \tag{3}$$

$$P = \frac{M}{2\beta_P}, \quad M = 8\frac{k_0\alpha_\infty}{\phi\Lambda^2}, \tag{4}$$

and for thermal dissipation,

$$\tilde{K}_{\text{eq}} = \frac{\gamma P_0}{\phi}\frac{1}{\tilde{\beta}(\omega)}, \quad \tilde{\beta}(\omega) = \gamma - (\gamma - 1)\left[1 + \frac{1}{\mathrm{j}\bar{\omega'}}\tilde{F'}(\omega)\right]^{-1}, \tag{5}$$

$$\tilde{F'}(\omega) = \sqrt{1 + \frac{M'}{2}\mathrm{j}\bar{\omega'}}, \quad \bar{\omega'} = \omega\rho_f \frac{k_0' C_P}{\kappa\phi}, \tag{6}$$

$$M^{'} = \frac{8k_0'}{\phi\Lambda'}. \tag{7}$$

The parameters used in this model relate to the micro-structure of the porous sample: porosity ϕ and tortuosity α_∞; viscous and thermal permeabilities k_0 and k_0'; characteristic viscous and thermal lengths Λ and Λ', respectively. Using the hypotheses of a log-normal pore distribution and a circular pore shape, it is possible to use only three parameters, namely the porosity ϕ, mean pore size $\bar{s}$ and pore size standard deviation σ_s (normalized by $\log(\bar{s})$), instead of six [34]. The relationships between the JCAPL and Horoshenkov model parameters are [34, 39] (there is a typo in the definition of β_P in Ref. [34], which was reproduced in our earlier work [40]):

$$\begin{aligned}
&\phi = \phi, \quad \alpha_\infty = e^{4(\sigma_s \log 2)^2}, \\
&k_0 = \frac{\bar{s}^2\phi}{8\alpha_\infty} e^{-6(\sigma_s \log 2)^2}, \quad k_0' = \frac{\bar{s}^2\phi}{8\alpha_\infty} e^{+6(\sigma_s \log 2)^2} \\
&\Lambda = \bar{s} e^{-\frac{5}{2}(\sigma_s \log 2)^2}, \quad \Lambda' = \bar{s} e^{+\frac{3}{2}(\sigma_s \log 2)^2} \\
&\beta_P = \frac{4}{3} e^{4(\sigma_s \log 2)^2} - 1.
\end{aligned} \tag{8}$$

The main reasons for the choice of using the Horoshenkov hypotheses are the simplicity of the model (few parameters) and its use of a statistical representation of the pore geometry. Having fewer parameters can greatly reduce the complexity of an inverse problem and prevent overfitting. This statistical representation of the pores is also thematically relevant to the use of a statistical (Bayesian) inference method.

Because of the wide variety of areas of application for the inverse characterization of the intrinsic properties of porous media, it also seems valuable to use a model whose properties (pore size and standard deviation) have a straightforward meaning to the end user, contrary to the JCAPL model properties.

The approach followed in this work does not require the use of a particular model for the identification, and could be straightforwardly attempted with simpler or more complex models.

2.2 Transfer matrix approach for multi-layer samples

A widespread technique to obtain the surface impedance of a multi-layer material is the transfer matrix method [41, Chap. 11], assuming the layers are all isotropic and only plane waves are propagated. Each individual isotropic layer is attributed a matrix, linking the acoustic field vector on one side of the layer to that at the other end of the layer. One can then multiply each individual matrix to obtain the acoustic field on the top surface of the stacked layers, in contact with the incident wave. This allows one to calculate the total reflection coefficient (or surface impedance) of the multi-layer material.

The method is used for combinations of rigid porous materials and air-gaps. Although not suited for very large samples or very high frequencies because of instability problems (see, i.e., Ref. [42]), it is in practice suitable for most, if not all, of the studies that would be performed in an impedance tube.

For a multi-layer material composed of N_S samples (including the air-gap) and with a rigid wall boundary condition (BC), the acoustic field in front of the sample writes

$$\begin{bmatrix} p \\ v \end{bmatrix}_{x=0} = \boldsymbol{I}_{0,1} \times \tilde{\boldsymbol{T}}^{(1)} \times \boldsymbol{I}_{1,2} \times \tilde{\boldsymbol{T}}^{(2)} \times \ldots \times \boldsymbol{I}_{N_S-1,N_S} \times \tilde{\boldsymbol{T}}^{(N_S)} \times \underbrace{\begin{bmatrix} 1 \\ 0 \end{bmatrix}}_{\text{rigid BC}}, \tag{9}$$

where p is the acoustic pressure, v the acoustic particle normal velocity. In the case where the rigid wall condition is not perfect, say it has an impedance $\Pi \neq +\infty$, the rigid BC array at the right of Eq. 9 becomes $\begin{bmatrix} 1 \\ \Pi^{-1} \end{bmatrix}$. In practice, one should characterize the impedance tube and try to obtain Π as high as possible. The abscissa $x = 0$ indicates the multi-layer surface in contact with the incident wave, and

$$\tilde{\boldsymbol{T}}^{(i)} = \begin{bmatrix} \cos\left(\tilde{k}_{\mathrm{eq}}^{(i)} L_i\right) & \mathrm{j} \cdot \sin\left(\tilde{k}_{\mathrm{eq}}^{(i)} L_i\right) \tilde{z}_{\mathrm{eq}}^{(i)} \\ \mathrm{j} \cdot \sin\left(\tilde{k}_{\mathrm{eq}}^{(i)} L_i\right) / \tilde{z}_{\mathrm{eq}}^{(i)} & \cos\left(\tilde{k}_{\mathrm{eq}}^{(i)} L_i\right) \end{bmatrix}, \quad \boldsymbol{I}_{i-1,i} = \begin{bmatrix} 1 & 0 \\ 0 & \frac{\phi_i}{\phi_{i-1}} \end{bmatrix} \tag{10}$$

are the transfer matrix of layer i and interface matrix between layers $i-1$ and i, respectively. This interface matrix translates the conservation of the volume of air at the interface, $\phi_{i-1} v_{i-1} = \phi_i v_i$. The equivalent wave number of the material is $\tilde{k}_{\mathrm{eq}}^{(i)} = \omega \sqrt{\tilde{\rho}_{\mathrm{eq}}^{(i)} / \tilde{K}_{\mathrm{eq}}^{(i)}}$ and $\tilde{z}_{\mathrm{eq}}^{(i)} = \sqrt{\tilde{\rho}_{\mathrm{eq}}^{(i)} \tilde{K}_{\mathrm{eq}}^{(i)}}$ is its equivalent characteristic impedance. Note that for an air-gap, the typical properties of air are used. The interface matrix $\boldsymbol{I}_{0,1}$ assumes $\phi_0 = 1$.

Next, the normalized surface impedance $\tilde{Z}_s(\omega)$ and the reflection coefficient $\tilde{R}(\omega)$ simply are

$$\tilde{Z}_s(\omega) = \frac{p_{x=0}}{v_{x=0}} \cdot \frac{1}{Z_f}, \quad \tilde{R}(\omega) = \frac{\tilde{Z}_s(\omega) - 1}{\tilde{Z}_s(\omega) + 1}, \tag{11}$$

with Z_f the characteristic impedance of air.

3 A source of bias in material characterization

3.1 Experimental apparatus

An impedance tube is a device made up of a loudspeaker connected to a tube, ending with a rigid backing. Porous materials are placed at the end of the tube, and microphones are located along the tube. The goal is to use the pressure measurements to separate the incident and reflected waves from the standing wave pattern created within the tube. A schematic of the tube is shown in Fig. 1.

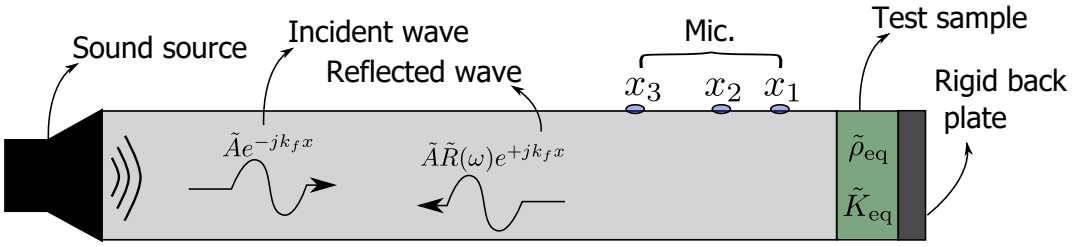

Figure 1: Schematics of an impedance tube

The pressure measured at the microphone locations x_i can then be obtained, provided that the source coefficient $\tilde{A}$ of the loudspeaker is known. The acoustic pressure p inside the impedance tube is, for plane waves,

$$p(x, \omega) = \tilde{A} e^{-\mathrm{j}k(\omega)x} + \tilde{A}\tilde{R}(\omega) e^{+\mathrm{j}k(\omega)x}, \tag{12}$$

with j the imaginary unit, x the longitudinal microphone locations in the tube and where $k(\omega) = \omega / c_f$ is the propagation wavenumber of air for the plane wave (here the tube is assumed wide enough to neglect viscous effects at the walls), with c_f the speed of sound.

The reflection coefficient is obtained by the solving of a linear system, since there is more information (three pressure measurements) than there are unknowns ($\tilde{A}$ and $\tilde{R}$), i.e., one has to solve for $Q = \left[\tilde{A}, \tilde{R}\right]^t$ in

$$\begin{bmatrix} p_1 \\ p_2 \\ p_3 \end{bmatrix} = \begin{bmatrix} e^{-\mathrm{j}k(\omega)x_1} & e^{+\mathrm{j}k(\omega)x_1} \\ e^{-\mathrm{j}k(\omega)x_2} & e^{+\mathrm{j}k(\omega)x_2} \\ e^{-\mathrm{j}k(\omega)x_3} & e^{+\mathrm{j}k(\omega)x_3} \end{bmatrix} \cdot Q, \tag{13}$$

where the notation $p_i = p(x_i, \omega)$ is used.

Note that this approach is not always followed. It is sometimes found in the literature that pressure measurements are used in pairs to identify the reflection coefficient, the pair being selected only at certain frequencies related to the spacing between the microphones [43]. Although this is justified when only two microphones are available, we argue that using all microphones simultaneously is strictly better. Indeed, provided that the linear system 13 is properly conditioned, no part of the available signal is wasted. For the proper placement of microphones, guidelines are provided in Ref [43]. Using more microphones can allow for the calculation of the impedance when in the presence of higher order modes, which propagates at higher frequencies.

3.2 Evaluating the uncertainty on the reflection coefficient

Using the transfer matrix method of Ref. [41, Chap. 11], the total reflection coefficient $\tilde{R}(\omega)$ can be calculated at normal incidence for a sample, with or without an air-gap.

Typically, one knows with which degree of uncertainty the pressure measurements are realized at the microphone of the impedance tube (say, 0.5 dB on the amplitude and 1° on the phase in the frequency band of interest). This error is usually a function of the frequency and averaging time. Here, for simplicity, it is assumed that a long enough averaging time is taken and that the remaining error is constant across all frequencies.

Numerical experiment: Let us consider a given uncertainty on the real and imaginary parts of microphone pressure measurements for a given reflection coefficient. Then, let us see what this uncertainty would become once re-propagated onto the calculated reflection coefficient (thus numerically mimicking an experiment). The following steps are performed successively at each frequency of interest :

- select a value of the reflection coefficient $\left\{\tilde{R}(\omega) \in \mathbb{C},\ \left|\tilde{R}(\omega)\right| \leq 1\right\}$, fix $\tilde{A} = 1$
- calculate the pressure p_i, $i = 1, 2, 3$ at the three microphone locations x_i, $i = 1, 2, 3$ using Eq. 12. The distance between microphones i and k is noted $d_{i,k}$: $d_{1,2} = 10\,\mathrm{mm}$, $d_{2,3} = 70\,\mathrm{mm}$.
- add a random Gaussian noise to the three pressure measurements, with standard deviation $\sigma = 0.05$ on both the real and imaginary parts, i.e.,
  - $\epsilon_{\Re,i} \sim \mathcal{N}(0, \sigma), \quad \epsilon_{\Im,i} \sim \mathcal{N}(0, \sigma) \Longrightarrow p(x_i) = p(x_i) + \epsilon_{\Re,i} + \mathrm{j}\epsilon_{\Im,i}, \quad i = 1, 2, 3$
- obtain the reflection coefficient from the noisy pressure measurements using Eq. 13.

The previous steps are repeated 10^4 times at each frequency for each value of the reflection coefficient, to provide converged statistics. In particular, we are interested in the standard deviation of the error on both the real and imaginary parts of the reflection coefficient calculated from the noisy signals. These are shown for some frequencies of interest in Fig. 2.

Interestingly, the standard deviations of the real and imaginary parts display a similar trend at a given frequency. However, the uncertainty on the reflection coefficient is clearly frequency

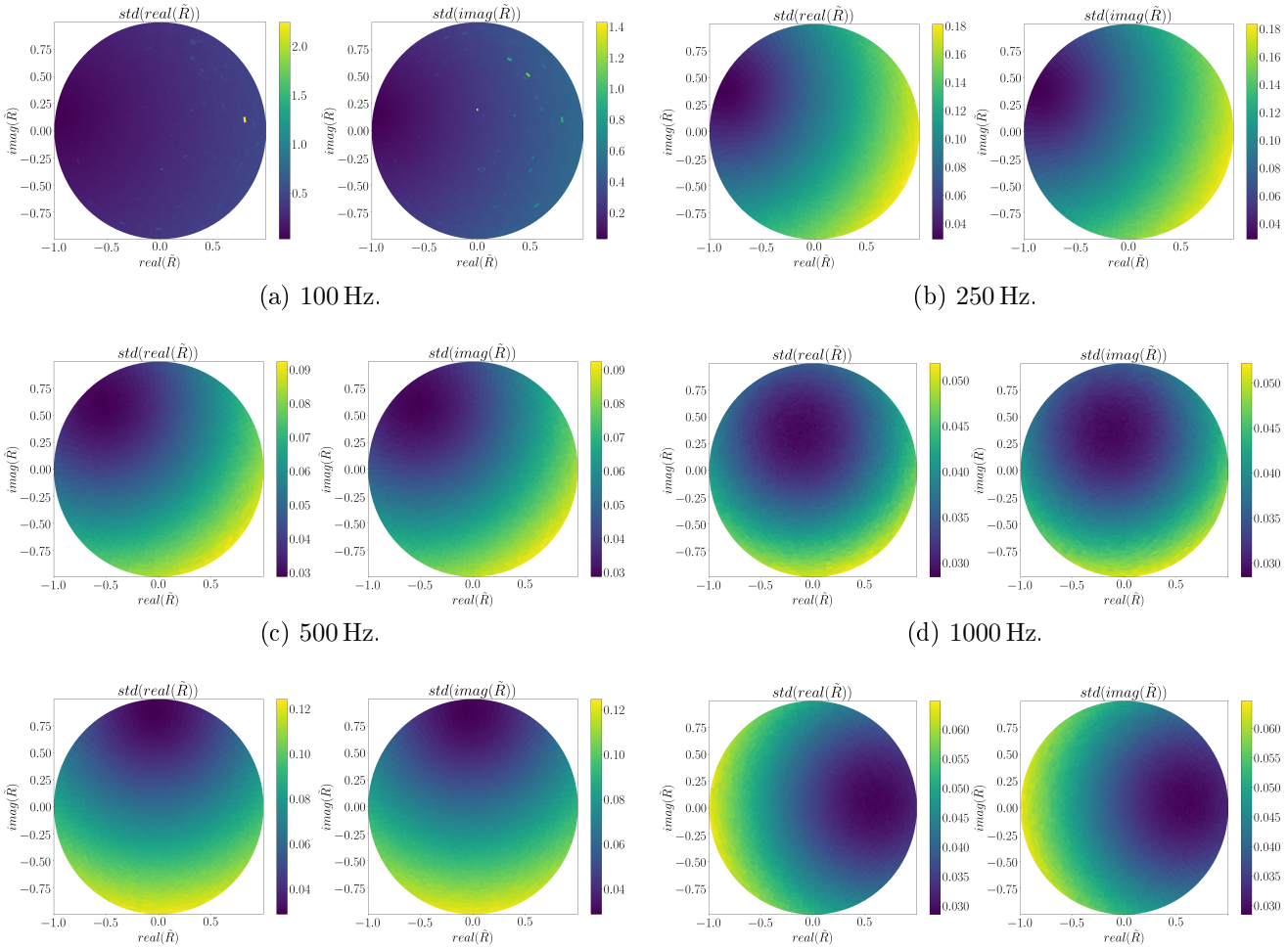

(a) 100 Hz. (b) 250 Hz.

(c) 500 Hz. (d) 1000 Hz.

(e) 2000 Hz. (f) 4000 Hz.

Figure 2: Standard deviation of the real (left) and imaginary (right) parts of the reflection coefficient.

dependent, and depends on the reflection coefficient value as well. This makes any inference approach based on the reflection coefficient an unnecessarily complex process, since one would have to give a value of the uncertainty at each frequency, for each value of the reflection coefficient. This also requires that one perfectly knows the microphone measurement uncertainty. If this is not done, and one takes an average uncertainty, then one would inevitably bias the identification by giving more weight to areas with high uncertainties, and less weight to areas with low uncertainties. The same could be said about the impedance and the absorption coefficient, even more so with the impedance since its values are not bounded, thus creating even larger contrasts of uncertainties depending on the frequency and impedance value.

To prove the previous points, a numerical test is performed where the reflection coefficient and associated uncertainties are given in Fig. 3 for a single-layer porous material, whose acoustic behavior is governed by the model detailed in Sec. 2.1. Material properties are $\phi = 0.98$, $\bar{s} = 250\,\mu$m and $\sigma_s = 0.05$, which are properties close to those of a melamine foam. Two cases are considered, one with no air-gap, and one where an air-gap of 30 mm is placed between the material and the rigid backing plate of the impedance tube.

The uncertainty is important in both cases at low frequencies. This is caused by the limited microphone spacing ($\sup_{i,k} |d_{i,k}| = 80\,$mm) and the linear system becoming increasingly more ill-

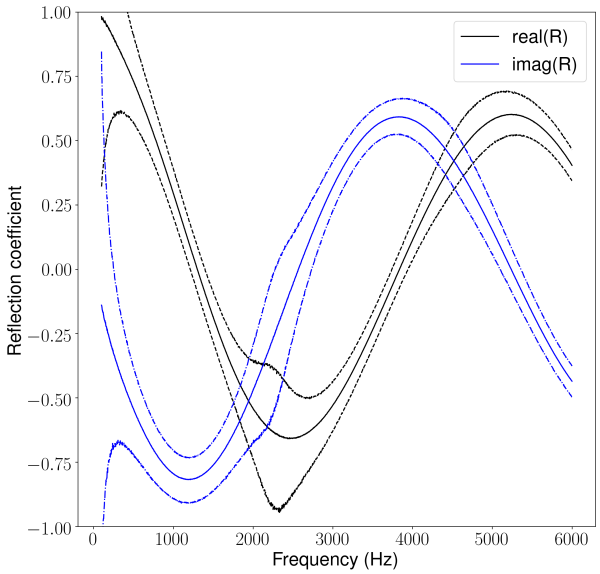

(a) Without an air-gap

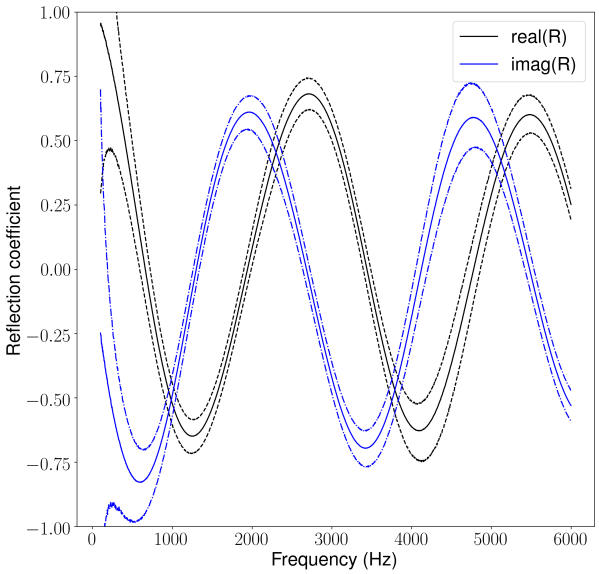

(b) With an air-gap of 30 mm placed behind the material

Figure 3: Real and imaginary parts of the reflection coefficient of a foam of thickness 30 mm with $\phi = 0.98$, $\bar{s} = 250\,\mu$m and $\sigma_s = 0.05$. The dashed lines correspond to the limits containing $\approx 95\%$ of the 10^4 samples that were used to obtain converged statistics.

conditioned, resulting in some cases in $\left|\tilde{R}\left(\omega\right)\right| > 1$. At around 2000 Hz, the uncertainty becomes large again only for the reference reflection coefficient with no air-gap present. Note that the error distribution does not necessarily always follow a normal distribution, because the mapping having the microphone pressures as input and the reflection coefficient as output is not linear. The main consequence of this test is that adding an air-gap may allow the experimenter to better observe parts of the signals, because of the uncertainty distribution in the observation with an additional air-gap being different from that in the reference no air-gap observation. Said differently, a frequency band can be shadowed in one experiment because of high uncertainties, and display small uncertainties when an air-gap has been added. This is caused by an air-gap changing the real and imaginary part of the reflection coefficient, which has a direct impact on the uncertainty, as shown in Fig. 2.

4 Bayesian inference for inverse identification of porous material properties

Given relevant indirect observations, one can use Bayes' theorem to update one's knowledge and draw conclusions about certain hypotheses. One of the tenets of the Bayesian approach to statistics is to interpret knowledge, or degree of belief, as a quantity represented by probabilities [44, Chap. 8].

This section presents the different elements required to perform the Bayesian inference of the model parameters of interest. The Bayesian inference approach used to find the posterior density functions of the parameters is recalled, as well as the specific numerical strategy.

4.1 Bayes' theorem

In Bayesian inference, knowledge on a parameter is represented by its probability density function. Bayes theorem on conditional probabilities writes

$$P\left(\theta|\mathcal{D},I\right)=\frac{P\left(\mathcal{D}|\theta\right)P\left(\theta,I\right)}{P\left(\mathcal{D},I\right)}, \tag{14}$$

where θ represents the model parameters to identify, $\mathcal{D}$ represents the observed data (real and imaginary parts of microphone pressure measurements), and I represents background general information, such as the choice of model (for the porous wave propagation and for the noise on the observed data). The goal is to sample from $P\left(\theta|\mathcal{D},I\right)$, the *posterior* probability, to reconstitute the probability density function (pdf) of each parameter. The *likelihood* $P\left(\mathcal{D},I|\theta\right)=\mathcal{L}\left(\theta\right)$ represents the mismatch between the model and the data for a given set of model parameters. Since a Gaussian hypothesis is made regarding the error on the pressure measurements (assumed distinct and independent for the real and imaginary parts of the signals, but constant across the microphones), one can write the likelihood as the product of likelihoods for the real and imaginary parts of the observations:

$$\mathcal{L}\left(\theta\right)=\left(2\pi\sigma_{\mathfrak{R}}\right)^{-N/2}e^{-\frac{S_{\mathfrak{R}}}{2\sigma_{\mathfrak{R}}^2}}\times\left(2\pi\sigma_{\mathfrak{I}}\right)^{-N/2}e^{-\frac{S_{\mathfrak{I}}}{2\sigma_{\mathfrak{I}}^2}}, \tag{15}$$

$$S_{\mathfrak{R}}=\sum_{k=1}^{N_{\text{micro}}}\sum_{n=1}^{N_{\text{freq}}}\text{real}\left(p_{k,n}^{\text{obs}}-p_{k,n}^{\text{num}}\right)^2,\quad S_{\mathfrak{I}}=\sum_{k=1}^{N_{\text{micro}}}\sum_{n=1}^{N_{\text{freq}}}\text{imag}\left(p_{k,n}^{\text{obs}}-p_{k,n}^{\text{num}}\right)^2, \tag{16}$$

where N is the number of measurement points ($N=N_{\text{freq}}\times N_{\text{micro}}$) with N_{freq} the number of frequencies contained in a signal and N_{micro} the number of microphones. The error standard deviations of the real and imaginary parts of the pressure measurements are denoted $\sigma_{\mathfrak{R}}$ and $\sigma_{\mathfrak{I}}$, respectively. This error is usually a function of the frequency and averaging time. Here, it is assumed that a long enough averaging time is taken and that the remaining error is constant across all frequencies. In the case of the present numerical study, this hypothesis is enforced and the exact synthetic signal is polluted with the addition of a Gaussian noise on its real and imaginary parts. Finally, $p_{k,n}^{\text{obs}}$ is the experimental pressure at the k^{th} microphone and n^{th} frequency, whereas $p_{k,n}^{\text{num}}$ is the numerical pressure evaluated with Eq. 12 after the reflection coefficient $\tilde{R}\left(\omega\right)$ was calculated using the transfer matrix approach (9,10,11), with parameters θ as input. Note that in practice, the logarithm of the likelihood is used to avoid numerical zeros.

The *prior* probability $P\left(\theta,I\right)$ represents all the information one may have on the parameters before the new measurement. For instance, one might have a precise measurement of the thickness of a sample, or an air-gap, and use the prior probability to encode this knowledge by a normal law of low standard deviation on the thickness parameter. Bayesian inference would then favor solutions respecting this added knowledge. In the present work, however, it was decided to not consider strong previous knowledge, to conduct a blind inference where only the acoustic data would drive the parameter inversion. It seemed more fitting, since only synthetic data generated with exactly known porous material properties are used, to not make things trivial by imposing a very tight parameter space during the inference. The parameter space is made of the Horoshenkov model parameters of the i^{th} porous sample, its thickness $L_{p,i}$, the temperature T and static pressure P_0 (used to calculate air properties, assuming an ideal gas law), the standard deviations $\sigma_{\mathfrak{R}}$ and $\sigma_{\mathfrak{I}}$ of the real and imaginary parts on the microphone pressure measurements, and the length of the j^{th} air-gap, $L_{a,j}$, if any. Uniform probabilities of broad supports are used for the prior to represent an initially uninformative state of knowledge, whose bounds are given in Table 1. The only exception is for the static pressure, for which a smaller relative prior support is chosen. This

is done because it is the only parameter that was shown to have close to zero influence on the identification, because of its low sensitivity in the test cases under study.

Table 1: Prior bounds of the parameters, where the symbol – means that there is no unit. The indices i and j denote the layer number and air-gap number, respectively. The $*$ exponent means the true value of a parameter.

Parameter	$\sigma_{\Re}$	$\sigma_{\Im}$	T	P_0	$L_{p,i}$	ϕ_i	$\bar{s}_i$	$\sigma_{s,i}$	$L_{a,j}$
Unit	Pa	Pa	°C	10^5 Pa	mm	–	μm	–	mm
Min	10^{-4}	10^{-4}	5	0.95	$0.5L^*_{p,i}$	0.1	10	0	1
Max	0.5	0.5	25	1.05	$1.5L^*_{p,i}$	0.999	10^3	0.99	100

Finally, $P(d_{\text{obs}})$ is the *evidence*, which represents the probability that a given model generated the observed data. In practice, the calculation of this term is avoided because of the need for a high dimensional integration. When the second level of Bayesian inference is needed, i.e., model selection [45], it becomes important to evaluate [27] or approximate [46, Chap. 2] the evidence. However, considerations of model selection are out of the scope of the present work.

Overall, Eq. 14 represents how the prior knowledge on the parameters is updated by the observation of new data $\mathcal{D}$, under certain hypotheses I. Only the first level of Bayesian inference is conducted, i.e., that of parameter identification. To obtain the posterior pdf of each parameter, a numerical approximation is obtained by the use of a Markov Chain Monte Carlo algorithm (MCMC, see Sec. 4.1.1).

4.1.1 MT_DREAM (ZS) approach to MCMC

The purpose of a Markov Chain Monte Carlo approach is to draw samples from an unnormalized distribution, such as the *posterior* pdf of Eq. 14 in our case, where the *evidence* term is not calculated. A Markov chain is created, which visits the (often high-dimensional) parameter space iteratively, jumping to a new position in space when a certain criterion is met. This rule of selection is given by the Metropolis-Hasting algorithm [47, 48], and can be summarized as follows:

- If the proposed position in space θ^{new} leads to an improvement in $P(\mathcal{D}|\theta)\,P(\theta, I)$, then the proposed value is accepted and stored in the chain.
- If the new position leads to a lower value of $P(\mathcal{D}|\theta)\,P(\theta, I)$, i.e. the parameters are less likely, then the proposed value is only accepted with a probability of $P(\mathcal{D}|\theta^{\text{new}})\,P(\theta^{\text{new}}, I)\,/P\left(\mathcal{D}|\theta^{\text{old}}\right)P\left(\theta^{\text{old}}, I\right)$ where θ^{old} is the previous value. If the proposed value is not accepted, the previous value is stored in the chain again.

The preceding means that the chain will move preferentially towards regions of high probability density, while allowing moves towards regions of lower density to properly explore the whole region of interest.

The main challenge of an MCMC approach lies in the proposal step, where a new position in the parameter space needs to be determined. If chosen randomly, there is a very little chance, in a high-dimensional space, that the point would be of any interest to the problem : it can easily fall too far off the region of interest, which has typically a small but unknown support, thus resulting in a lot of wasted numerical resources. This problem is coined as the curse of dimension. To palliate this issue, one strategy consists in using multiple chains in parallel that can learn from each other, in

a way similar to differential evolution techniques used in optimization [49]. The MCMC approach which is followed is the Multiple-Try DiffeRential Evolution Adaptive Metropolis with sampling from past State : MT_DREAM (ZS) [50–52], where Z is the name of the past state storage matrix . This strategy offers a lot of different techniques to mix the chains efficiently to explore high-dimensional space (snooker update, self-adaptive randomize subspace, differential evolution update), and was shown to work even in the case of multi-modal distributions (at least up to a dimension of 25 [52, Sec. 3.2] for a tri-modal Gaussian distribution with well separated modes). This latter point is of importance in the present study, as the multi-modality (presence of multiple peaks) in a posterior density is a sign of non-uniqueness of a solution : given the observation that has been realized, multiple parameter values are likely. Since a goal of the present work was to find a way to remove this non-uniqueness, it was chosen to use the MT_DREAM (ZS) approach to accurately explore the potentially multi-modal densities of the parameters.

In all the simulations that were performed, three chains were ran in parallel, with $3 \cdot 10^5$ iterations and 3 tries for each iteration (the proposal was a combination of multiple tries). To check the convergence of the chains, a Gelman-Rubin criterion was used [53], yielding values lower than 1.01 for all parameters except for those presenting multi-modal distributions, where the criterion is not well-adapted and where we relied on the convergence of the other parameters and on visual checks of the chains. The MCMC python code implementation that was used is freely available under the GNU GPLv3 license at https://github.com/LoLab-VU, and was created by the Lopez Lab at Vanderbilt University [54].

5 Results

5.1 Description of the numerical tests

Three numerical materials were used, M_1, M_2 and M_3, whose properties are summarized in Table 2. Only the Horoshenkov properties are identified (ϕ, $\bar{s}$, σ_s) but the equivalent properties of the JCAPL model are given for information. In practice, here are the steps followed for the numerical

Table 2: Properties of the Horoshenkov model and derived properties for materials M_1, M_2, M_3

		Horoshenkov model properties [34]		JCAPL model properties derived from Eq. 8					
Material	ϕ	$\bar{s}\,(\mu\mathrm{m})$	σ_s	α_∞	$k_0\,(\cdot 10^{-10}\,\mathrm{m}^2)$	$\Lambda\,(\mu\mathrm{m})$	$\Lambda'/\Lambda = \alpha_\infty$	k_0'/k_0	β_P
M_1	0.85	100	0.2	1.08	8.77	95.3	1.08	1.26	0.44
M_2	0.65	50	0.5	1.62	0.61	37.0	1.62	4.23	1.16
M_3	0.98	250	0.05	1.0	75.6	249.3	1.0	1.01	0.34

study:

- A single or multi-layer material is chosen, with or without an air-gap, and the exact reflection coefficient is calculated by the transfer matrix approach (9,10,11).
- The *numerical* synthetic pressure inside the impedance tube is evaluated at $x_1 = 2\,\mathrm{cm}$, $x_2 = 3\,\mathrm{cm}$ and $x_3 = 10\,\mathrm{cm}$ (with $x = 0$ at the material upper surface) with Eq. 12 and fixing the source coefficient at $\tilde{A} = 1$.

- A Gaussian noise is added to the pressure signals to represent an experimental error/uncertainty, with $\sigma_{\Re} = 0.05$ and $\sigma_{\Im} = 0.08$ the standard deviations of the error on the real and imaginary parts of the signals, respectively. See Fig. 4 for a representation of this signal on the three microphone locations for material M_1 alone of thickness $L_1 = 30\,\text{mm}$, without an air-gap.

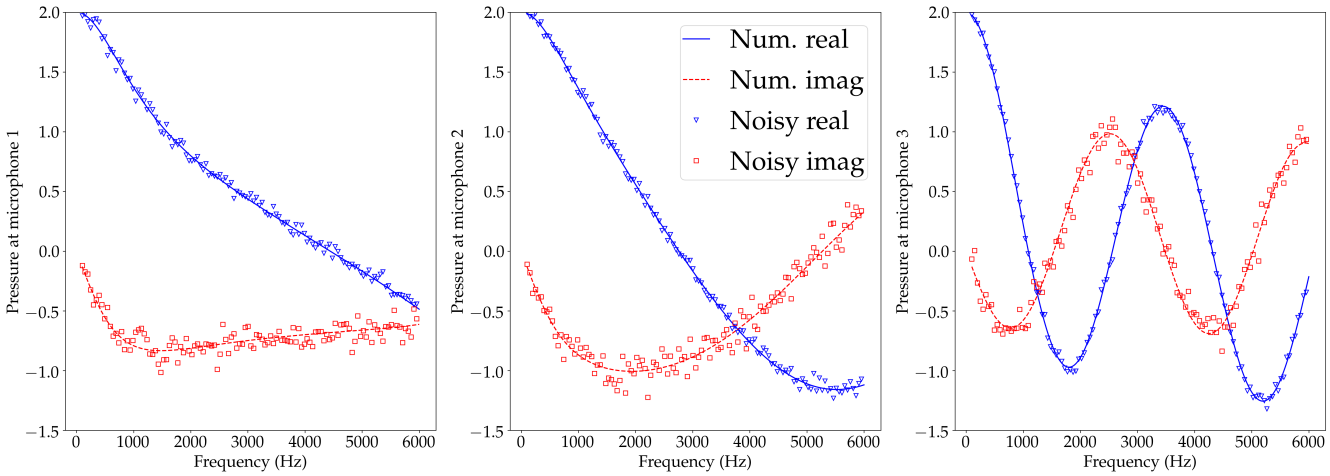

Figure 4: Microphone signals in the impedance tube for material M_1

- The noisy pressure signals are then used as input to the MT_DREAM(ZS) algorithm described in Sec. 4.1.1.

5.1.1 Inverse crime

The reader familiar with inverse problems will have noticed that in the current numerical analysis, the same model is used to generate the synthetic data and to infer the model parameters. This is sometimes referred to as an inverse crime [55], because of the more manageable aspect of the inverse problem in such cases (thus potentially hiding the true difficulty of the same approach on real experimental data). The addition of a Gaussian noise to pollute the signals partially removes the inverse crime, and, counter-intuitively, might even make the problem more tractable. Without noise, the likelihood has a very steep gradient at the true value of the parameters, which can make the exploration of the posterior densities more challenging and increase the occurence of multi-modal distributions (the equivalent of local minima when using a standard optimization approach to an inverse problem). It was chosen to follow a pragmatic approach, in adding a noise with a standard deviation between $5-8\%$ of the input signal amplitude $\tilde{A} = 1$ of the source wave. This is equivalent to having a standard deviation of about 0.5 dB for an incident wave amplitude of 94 dB, which is representative of typical microphone uncertainty specifications.

We note that in the limit where $\sigma_{\Re}$ or $\sigma_{\Im}$ is very high, no information can be drawn from the signals about the inferred parameters.

5.2 Discussion of the results

First, the Bayesian inference identification process is performed on each sample (whose thickness is fixed at 30 mm) individually, with or without air-gaps (see Figs. 5,6,7). This makes it possible to show how the method performs in a default situation with only one layer to identify. The identification of the six possible combinations of multi-layers made up of two single layers is then performed (see Figs. 8,9,10,11,12,13), followed by that of the six combinations of multi-layers

made up of three single layers (see Figs. 14,15,16,17,18,19). The total thickness of the multi-layer is always taken to be 30 mm (not including air-gap), distributed equally on all layers. A summary of the sample combinations that are identified is given in Table. 3.

Table 3: Summary of the 15 sample configurations and associated figures. The symbol $\circ$ means the stacking of materials, with the left term being the one closest to the acoustic source.

One layer		Two layers		Three layers	
Combination	Figure	Combination	Figure	Combination	Figure
M_1	5 on the following page	$M_1 \circ M_2$	8 on page 16	$M_1 \circ M_2 \circ M_3$	14 on page 23
M_2	6 on page 15	$M_2 \circ M_1$	9 on page 17	$M_2 \circ M_1 \circ M_3$	15 on page 24
M_2	7 on page 15	$M_1 \circ M_3$	10 on page 18	$M_1 \circ M_3 \circ M_2$	16 on page 25
		$M_3 \circ M_1$	11 on page 19	$M_3 \circ M_1 \circ M_2$	17 on page 26
		$M_2 \circ M_3$	12 on page 20	$M_2 \circ M_3 \circ M_1$	18 on page 27
		$M_3 \circ M_2$	13 on page 21	$M_3 \circ M_2 \circ M_1$	19 on page 28

For each of the 15 sample configurations, five different inferences are conducted, where the number of air-gaps and the number of frequencies in a signal are varied. The goal is to determine whether an improvement in the parameter identification is caused by the presence of air-gaps in the observation, or simply to the increase in the number of frequencies caused by the observation of additional signals. The cases are summarized in Table 4.

Table 4: Summary of the different observations used in each of the 15 sample configurations. The ✓ symbol means that the observation has been used for the inference. N_{freq} is the number of frequencies contained in a single signal, whereas N is the total number of data points used in Eq. 15.

Case	N_{freq}	No air-gap	Air-gap length			N
			2 cm	4 cm	6 cm	
1	1200	✓				1200
2	4800	✓				4800
3	1200	✓	✓			2400
4	1200	✓	✓	✓		3600
5	1200	✓	✓	✓	✓	4800

Even though parameters like the temperature or static pressure were identified during all the test cases, they are of relatively low importance to the study, the goal being that of recovering the material parameters. However, it was noted that the temperature was very well identified in all cases (i.e., displaying a posterior pdf of small support centered on the true value), showing a high sensitivity relative to the inverse problem. By contrast, the static pressure was always poorly identified, in the sense that the posterior density was almost uniform, over the entire support of

the prior, meaning that no information on the parameter could be gained. Other notable findings are that the noise parameters $\sigma_{\Re}$ and $\sigma_{\Im}$ were always correctly identified, as well as the air-gap lengths. The thickness of a sample was not always well identified in the multi-layer cases when the other parameters were also not well identified. This is caused by the thickness having a similar influence on the observed signals as the tortuosity $\alpha_\infty(\bar{s}, \sigma_s)$ of a sample, because of both of these parameters controlling partially the effective travel length of a wave inside the sample. This model correlation introduces difficulties in the identification, especially when multiple modes are present.

In the following, the 5 inference cases summarized in Table 4 are displayed in each figure. The displayed pdfs are obtained by taking the samples of the MCMC chains, removing the first 20% samples as burn-in (so that the chains properly reach the density to explore), and using the seaborn [56] python package for the plot of the kernel density estimate.

When the experiment is repeated with an air-gap, it would be counterproductive to reduce the number of frequencies in each signal to keep N constant, as less information would be drawn from the observation. However, case 2 was added to assess whether adding more frequencies in a single observation is equivalent to adding observations with an air-gap, in terms of parameter identification.

5.3 Mono-layer identifications

The identification of a single layer of porous material was successfully carried out, as shown in Figs. 5,6,7 where the posterior pdfs all display a support that is sensibly smaller than the prior support in Table 1.

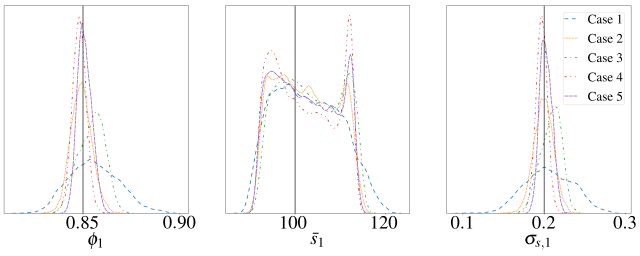

Figure 5: Posterior pdfs of the properties of material M_1. The black vertical line corresponds to the true value. The legend refers to Table 4

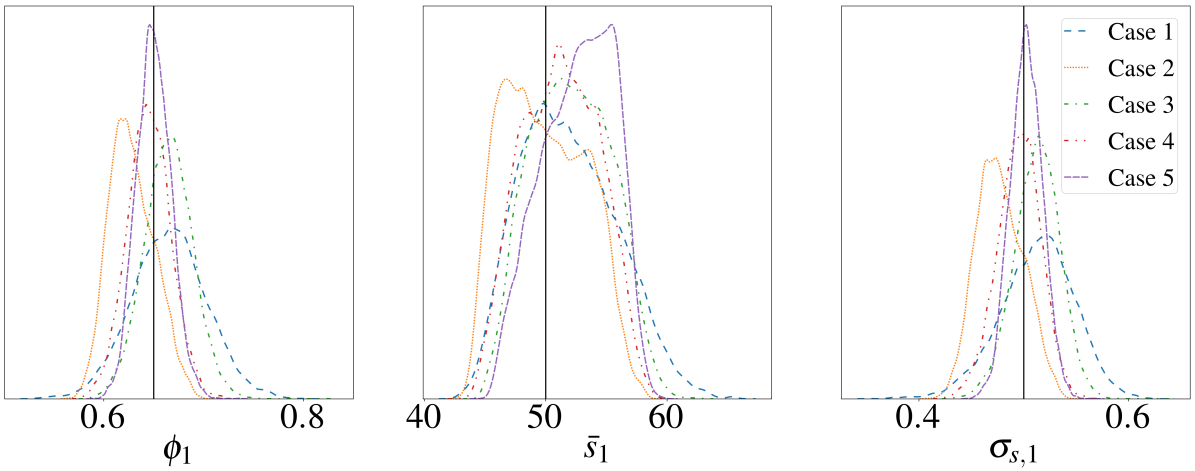

Figure 6: Posterior pdfs of the properties of material M_2. The black vertical line corresponds to the true value. The legend refers to Table 4

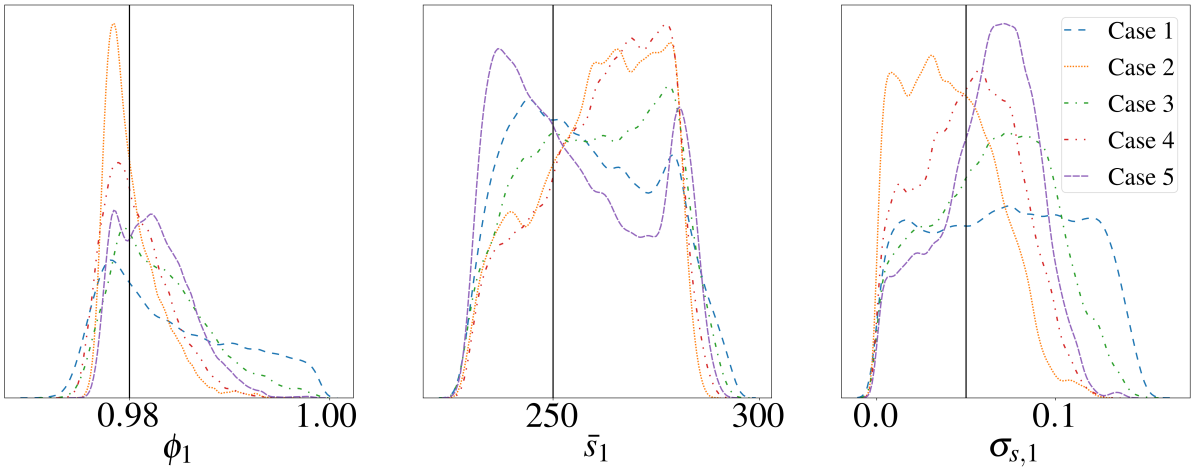

Figure 7: Posterior pdfs of the properties of material M_3. The black vertical line corresponds to the true value. The legend refers to Table 4

It is observed that the identification case 5 yields better identification results for materials M_1 and M_2 when compared with identifications cases 1 and 2, meaning that the posterior density is usually closer to the true value (vertical line) and has a narrower support. Since the pdfs are not normalized, a narrow support directly translates in the highest value of the pdf being higher than for broader pdfs.

Although it is no surprise that the reference identification (case 1) does not yield results as precise as those in the other cases because of the lower number of observations ($N = 1200$), the two cases 2 and 5 both have the same $N = 4800$. The only difference is that for case 5 the observations are split between four different numerical experiments of $N = 1200$ including three different air-gaps, instead of just one with $N = 4800$ with just the reference (no air-gap) observation.

This identification test on mono-layers is a first indication that diversifying the observation using air-gaps could in some cases increase the information content available on the parameters to identify. This improvement might be material dependent, as in the case of material M_3, where it does not seem worth the additional experiments. It is postulated that low resistivity materials (such as M_3) do no benefit as much from the addition of air-gaps because of the air-cavity

effect being less pronounced than for resistive materials. The different signals thus share a similar type of information content, and cannot be used as efficiently to improve one's knowledge on the parameters.

5.4 Bi-layer identification

The identification of a bi-layer of porous materials was successfully carried out, as shown in Figs. 8,9,10,11,12,13 where the posterior pdfs all display a support that is sensibly smaller than the prior support in Table 1.

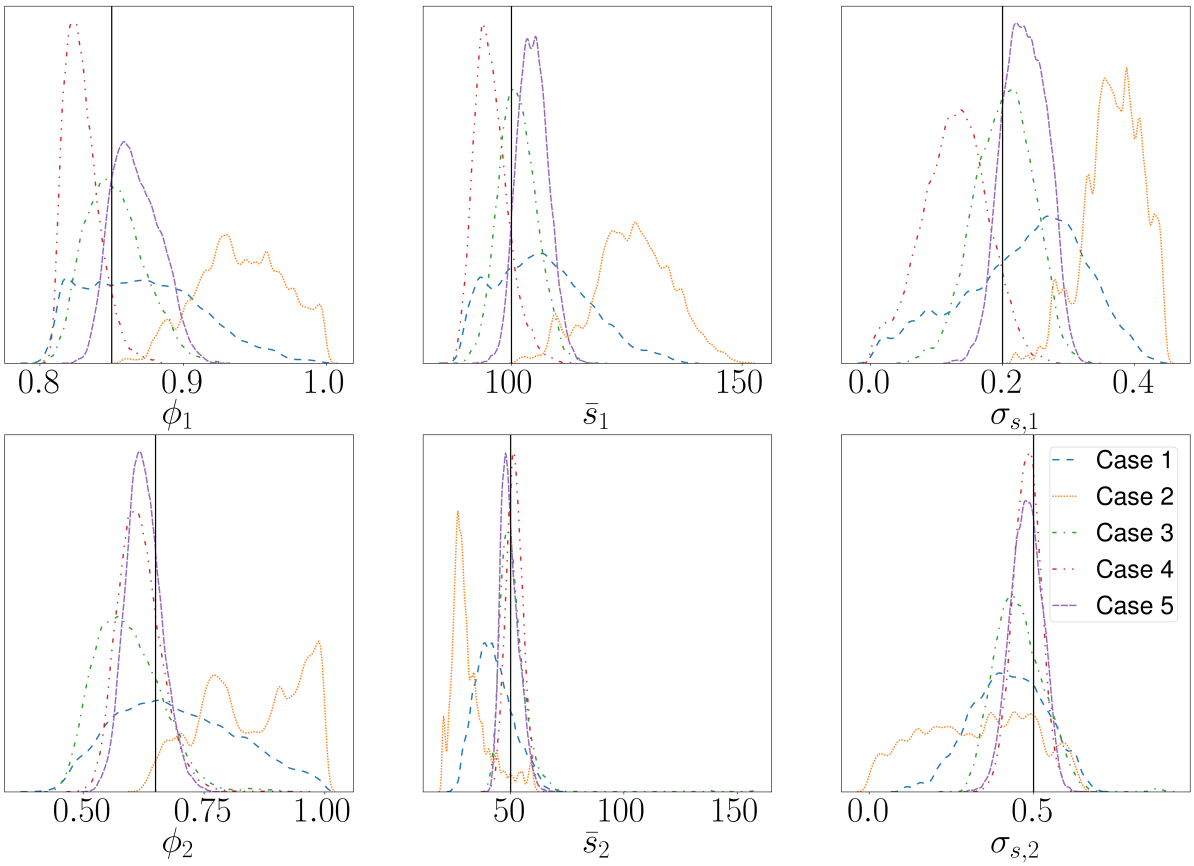

Figure 8: Posterior pdfs of the bi-layer $M_1 \circ M_2$. The black vertical line corresponds to the true value. The legend refers to Table 4

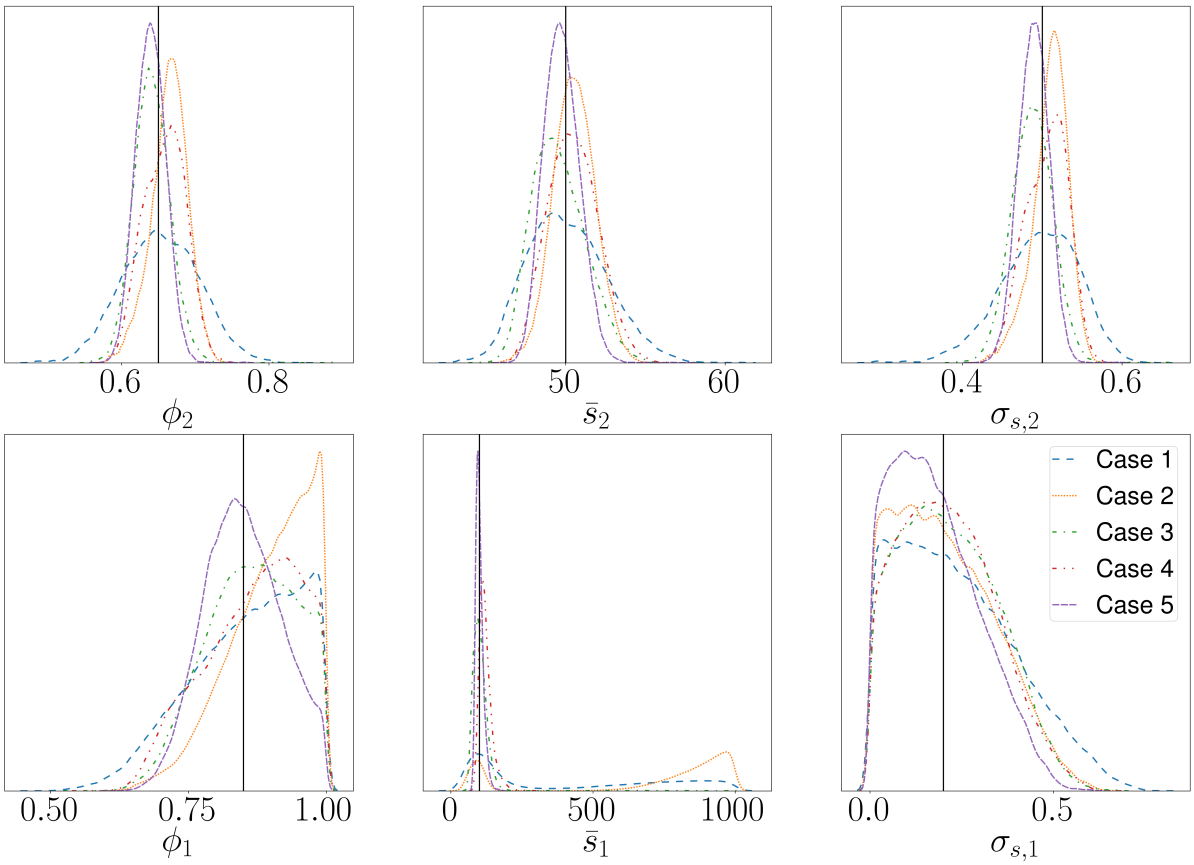

Figure 9: Posterior pdfs of the bi-layer $M_2 \circ M_1$. The black vertical line corresponds to the true value. The legend refers to Table 4

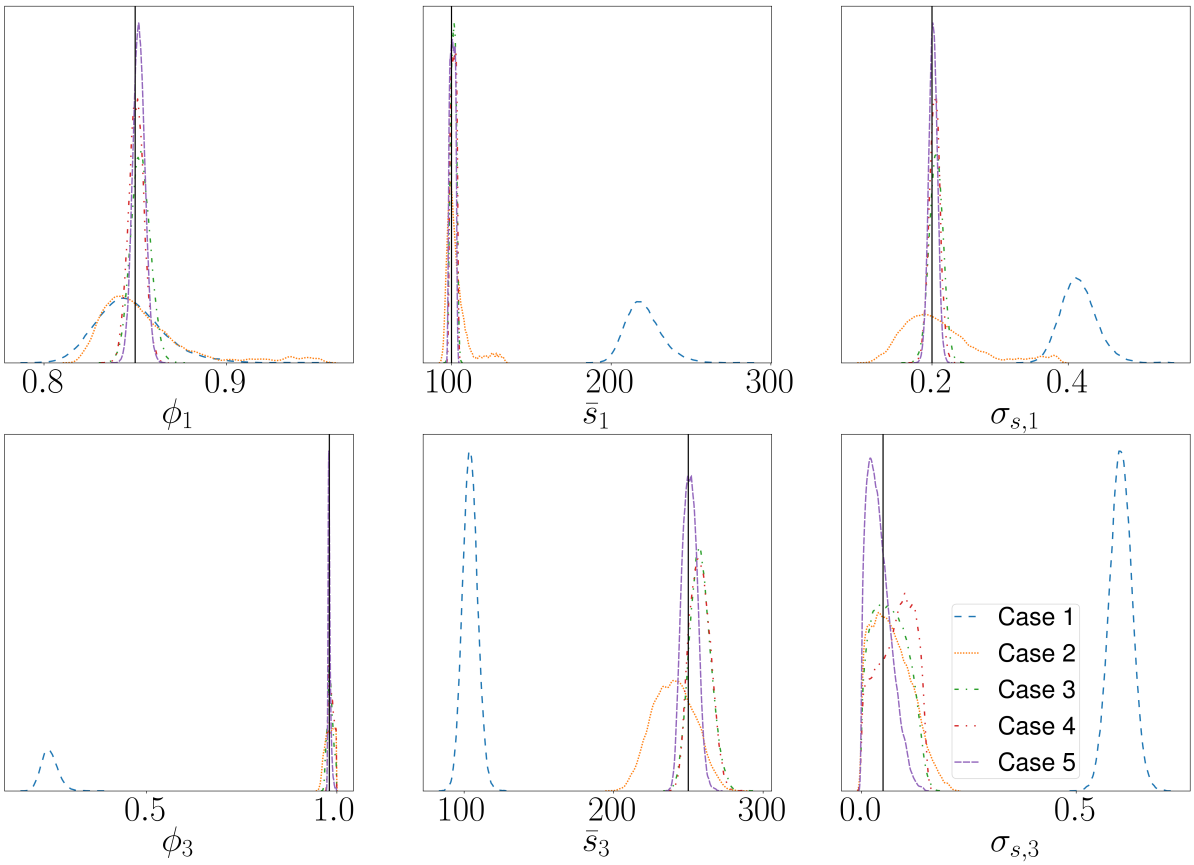

Figure 10: Posterior pdfs of the bi-layer $M_1 \circ M_3$. The black vertical line corresponds to the true value. The legend refers to Table 4

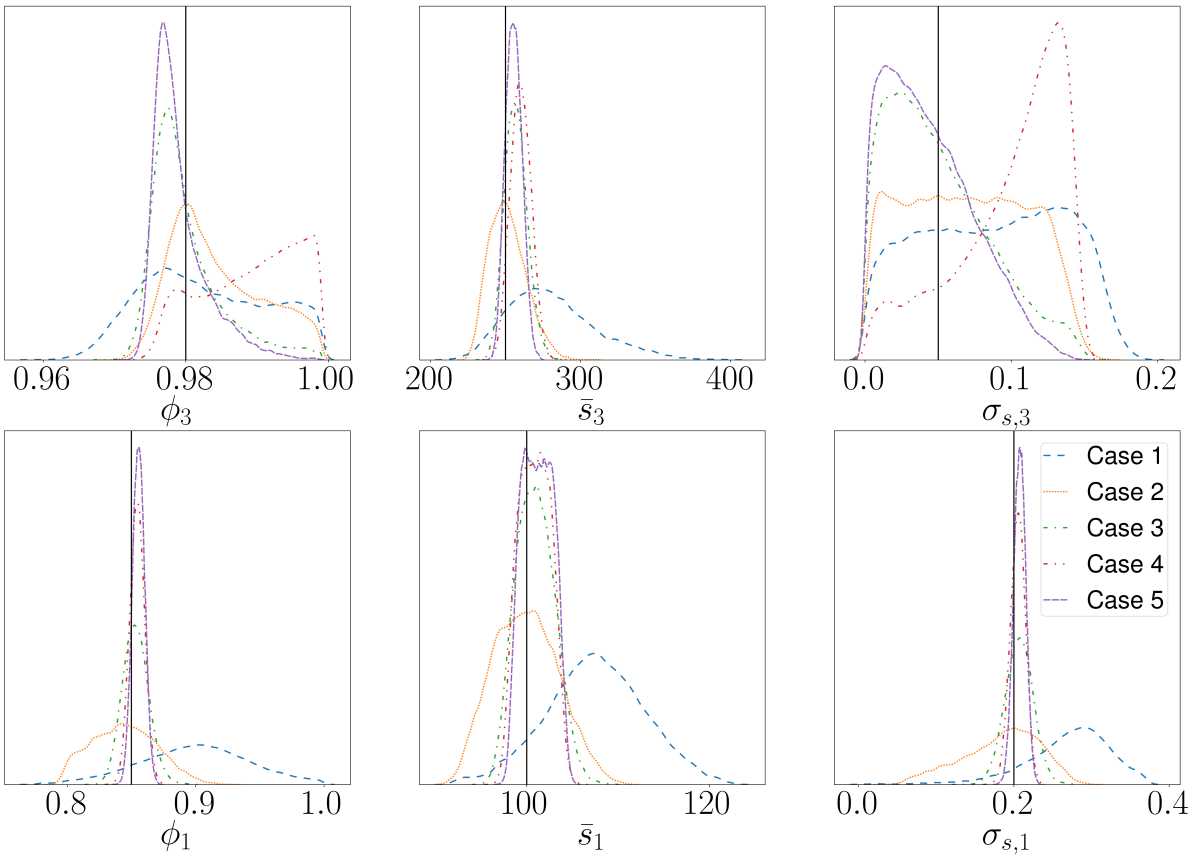

Figure 11: Posterior pdfs of the bi-layer $M_3 \circ M_1$. The black vertical line corresponds to the true value. The legend refers to Table 4

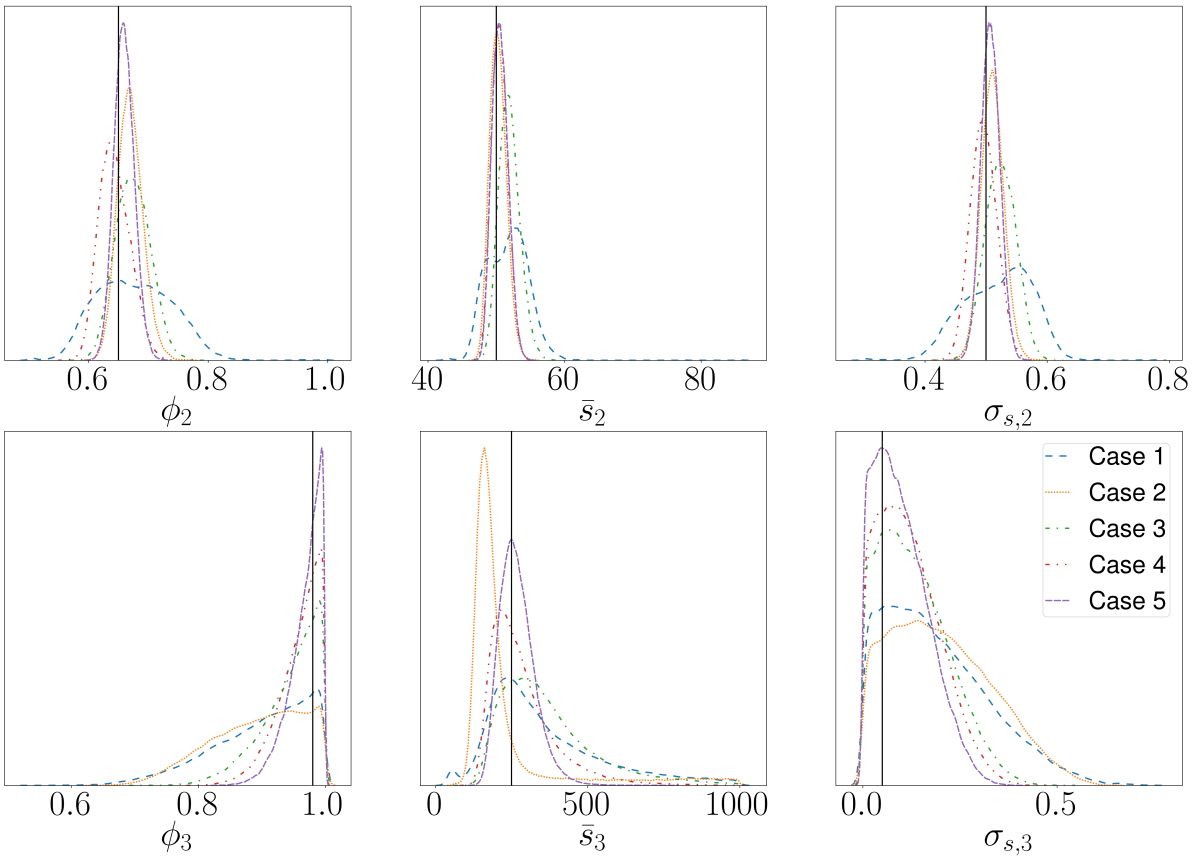

Figure 12: Posterior pdfs of the bi-layer $M_2 \circ M_3$. The black vertical line corresponds to the true value. The legend refers to Table 4

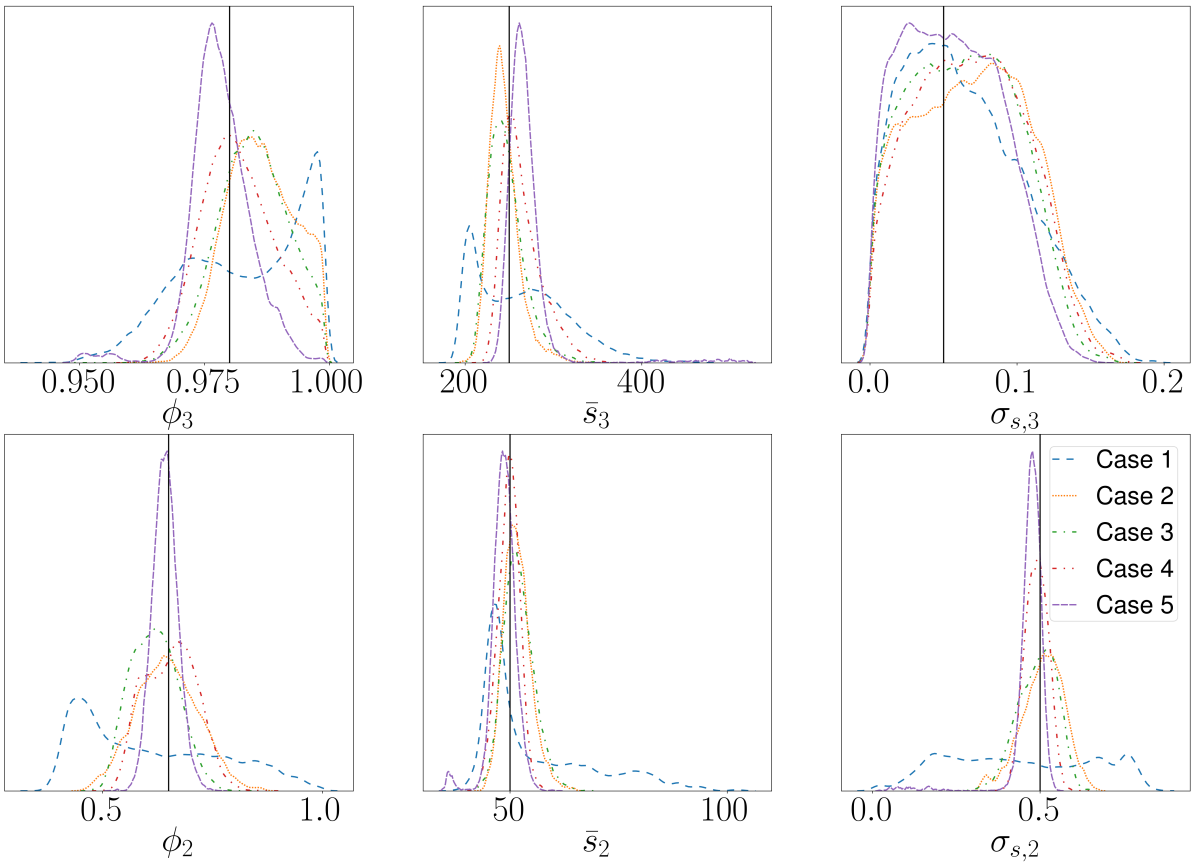

Figure 13: Posterior pdfs of the bi-layer $M_3 \circ M_2$. The black vertical line corresponds to the true value. The legend refers to Table 4

The main difference with the identification of a mono-layer is that ill-posedness starts to appear in the problem. For instance, in the identification of $M_2 \circ M_1$ in Fig. 9, the mean pore size of M_1, $\bar{s}_1$, presents a very wide posterior for case 1 and 2, with two peaks of density. In the identification of $M_1 \circ M_3$, the identification of case 0 fails altogether to retrieve the correct parameters.

Overall, the pdf supports are larger than in the case of mono-layer parameter identification, which was expected because of the increased complexity of the problem. Also, since the thickness of each layer is reduced, it stands to reason that each individual material has less influence on the observation than in the mono-layer case, thus causing a larger pdf.

It is observed that the identification case 5, including the presence of air-gaps, almost systematically provides the best identification of all the parameters (close to true value with a narrow support of the pdf). This is a strong indication that adding air-gaps behind materials in an impedance tube increases the information content available, thus providing better identification of material properties, even in the case of a bi-layer material.

Of importance for the identification is the ordering of the layers, as was also observed in Ref. [27]. If a resistive material is placed in front of another material, a lesser amount of the incident wave will reach the second layer and eventually be seen on the observed signals. For instance, in the identifications of the $M_1 \circ M_2$ (Fig. 8) and $M_2 \circ M_1$ (Fig. 9) bi-layers, identification of the former layer is easier than that of the latter, as seen by smaller pdf supports.

This limitation is intrinsic to the method, and is part of the reason why the thickness of each layer was halved in the bi-layer cases. It is indeed almost impossible to identify any multi-layer material using the present technique (or any other that we know of) when the first layer is made

of a large and/or very resistive material. The incident wave simply does not "see" enough of the subsequent layers to provide information on these layers within the observed signals.

Finally, it seems that a single additional observation with an air-gap is sufficient to retrieve most of the information and remove the non-uniqueness of the solution in the bi-layer case, whereas adding more air-gaps to make new observations can make the precision with which parameters are retrieved increase. The difference in parameter identification between using 2 air-gaps (3 observations) or 3 air-gaps (4 observations) is sometimes minimal, but cannot really be predicted in advance. It is thus advised to perform as many measurements as possible within the time constraints that one can allocate.

5.5 Tri-layer identification

The identification of a tri-layer of porous materials was successfully carried, as shown in Figs. 14,15,16,17,18,19 where the posterior pdfs all display a support that is sensibly smaller than the prior support of Table 1.

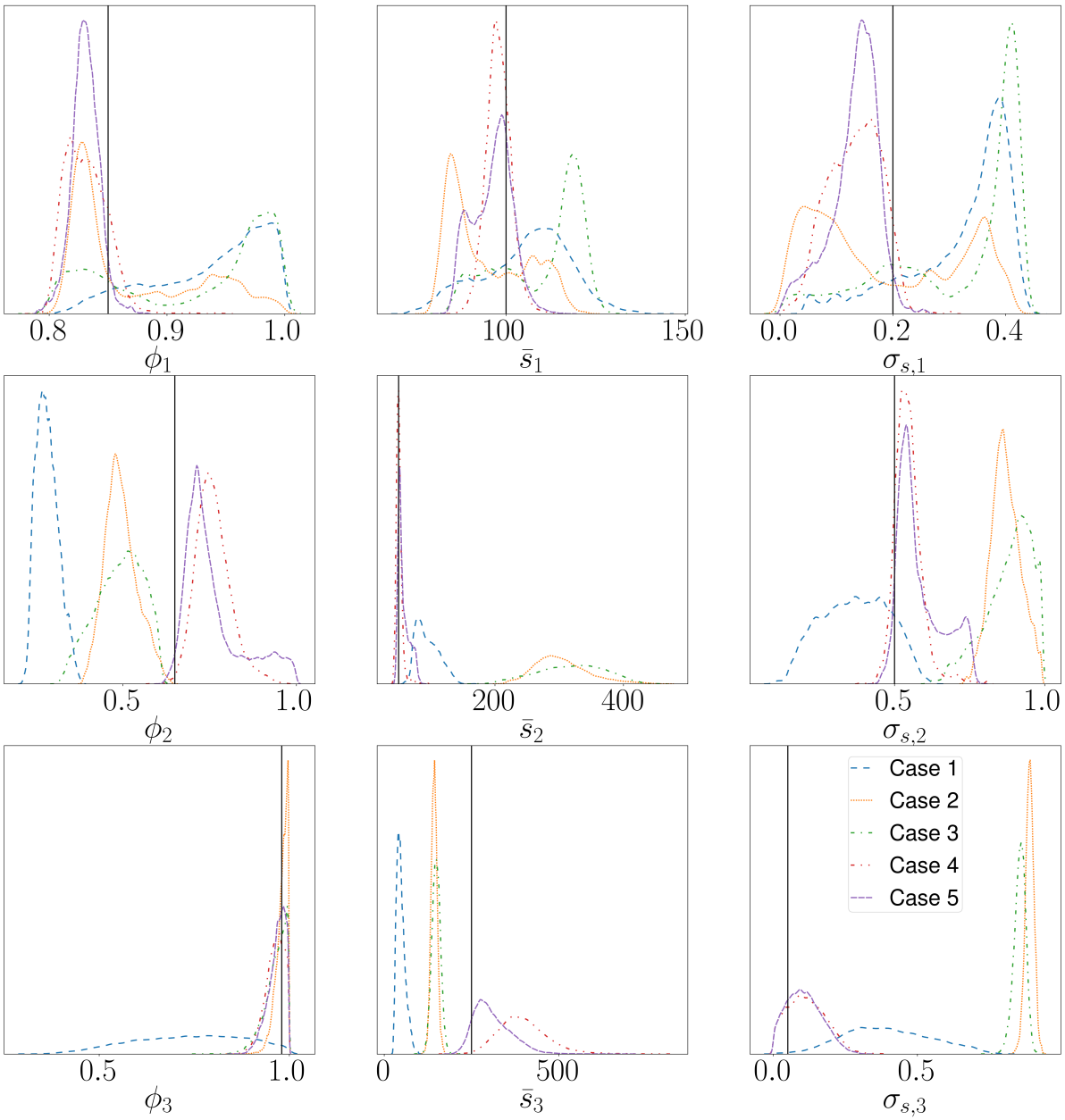

Figure 14: Posterior pdfs of the tri-layer $M_1 \circ M_2 \circ M_3$. The black vertical line corresponds to the true value. The legend refers to Table 4

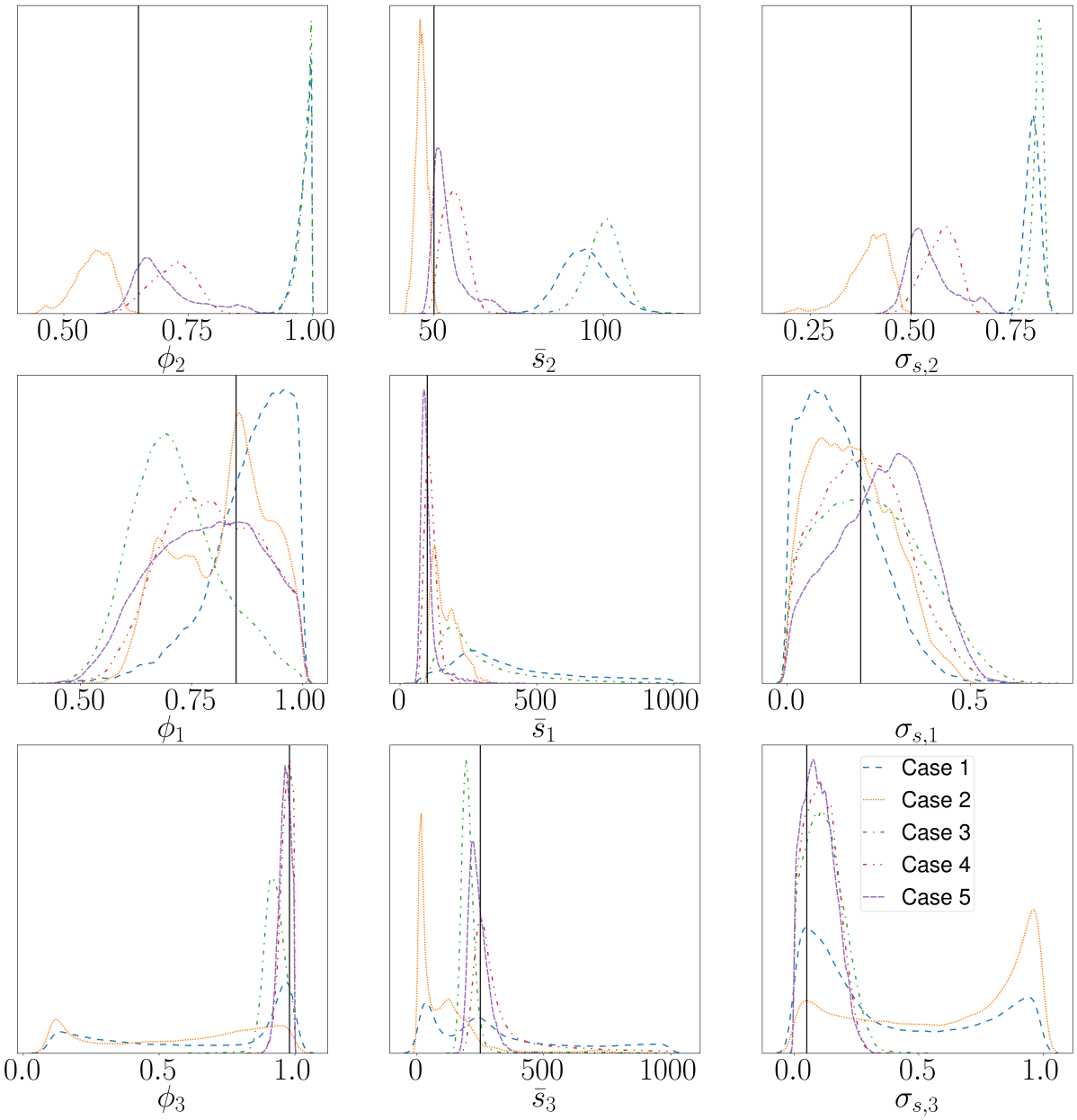

Figure 15: Posterior pdfs of the tri-layer $M_2 \circ M_1 \circ M_3$. The black vertical line corresponds to the true value. The legend refers to Table 4

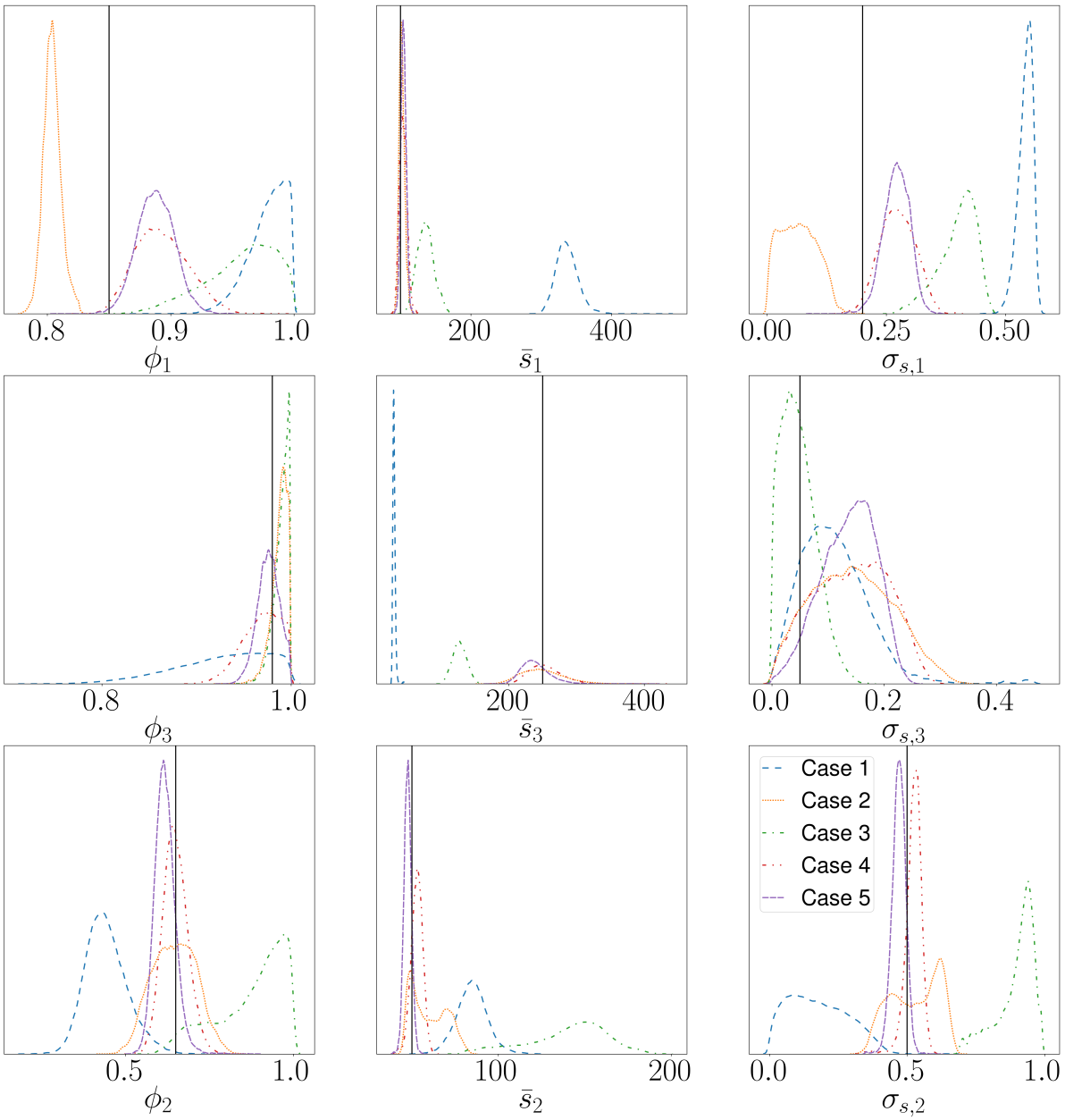

Figure 16: Posterior pdfs of the tri-layer $M_1 \circ M_3 \circ M_2$. The black vertical line corresponds to the true value. The legend refers to Table 4

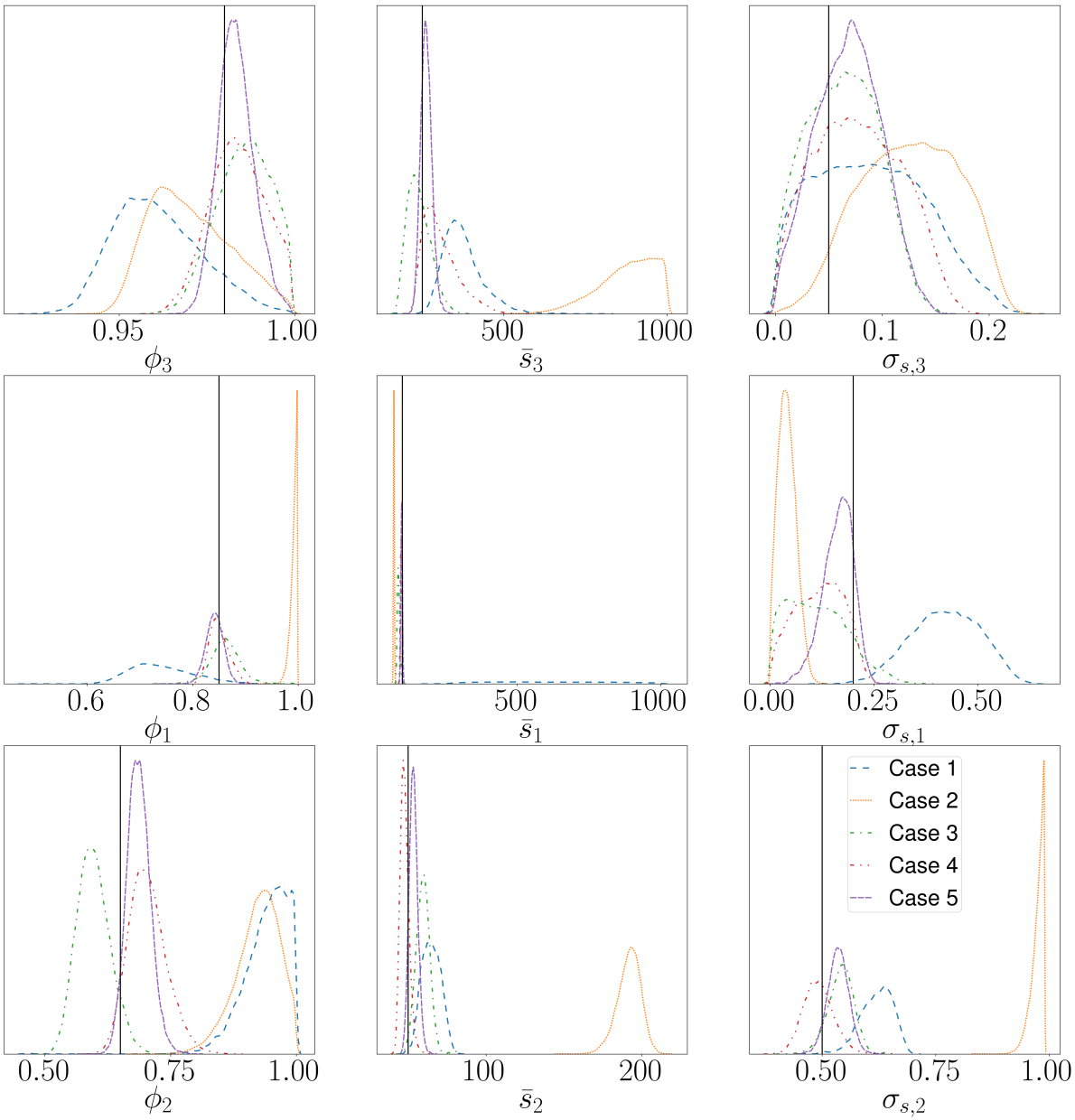

Figure 17: Posterior pdfs of the tri-layer $M_3 \circ M_1 \circ M_2$. The black vertical line corresponds to the true value. The legend refers to Table 4

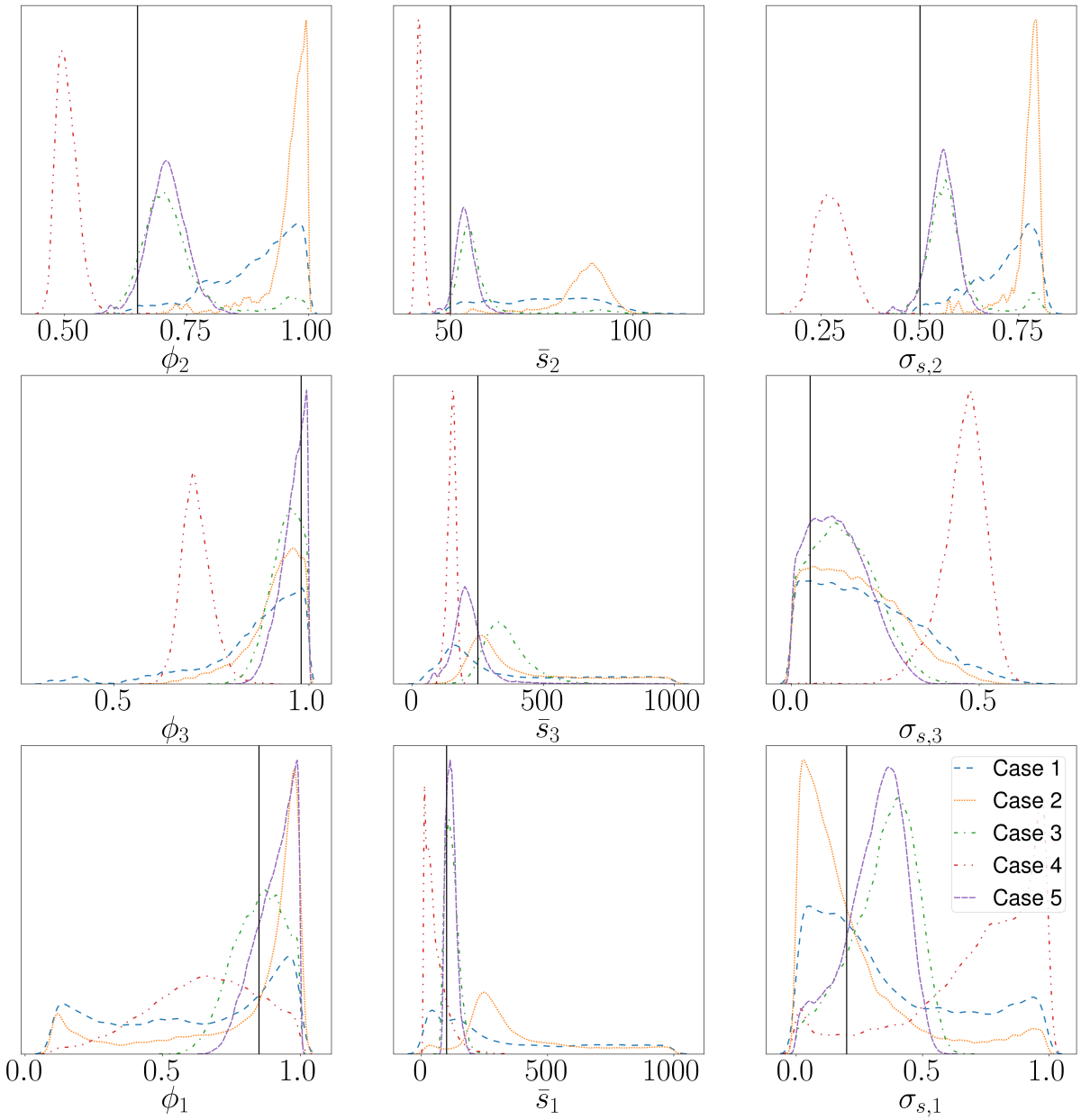

Figure 18: Posterior pdfs of the tri-layer $M_2 \circ M_3 \circ M_1$. The black vertical line corresponds to the true value. The legend refers to Table 4

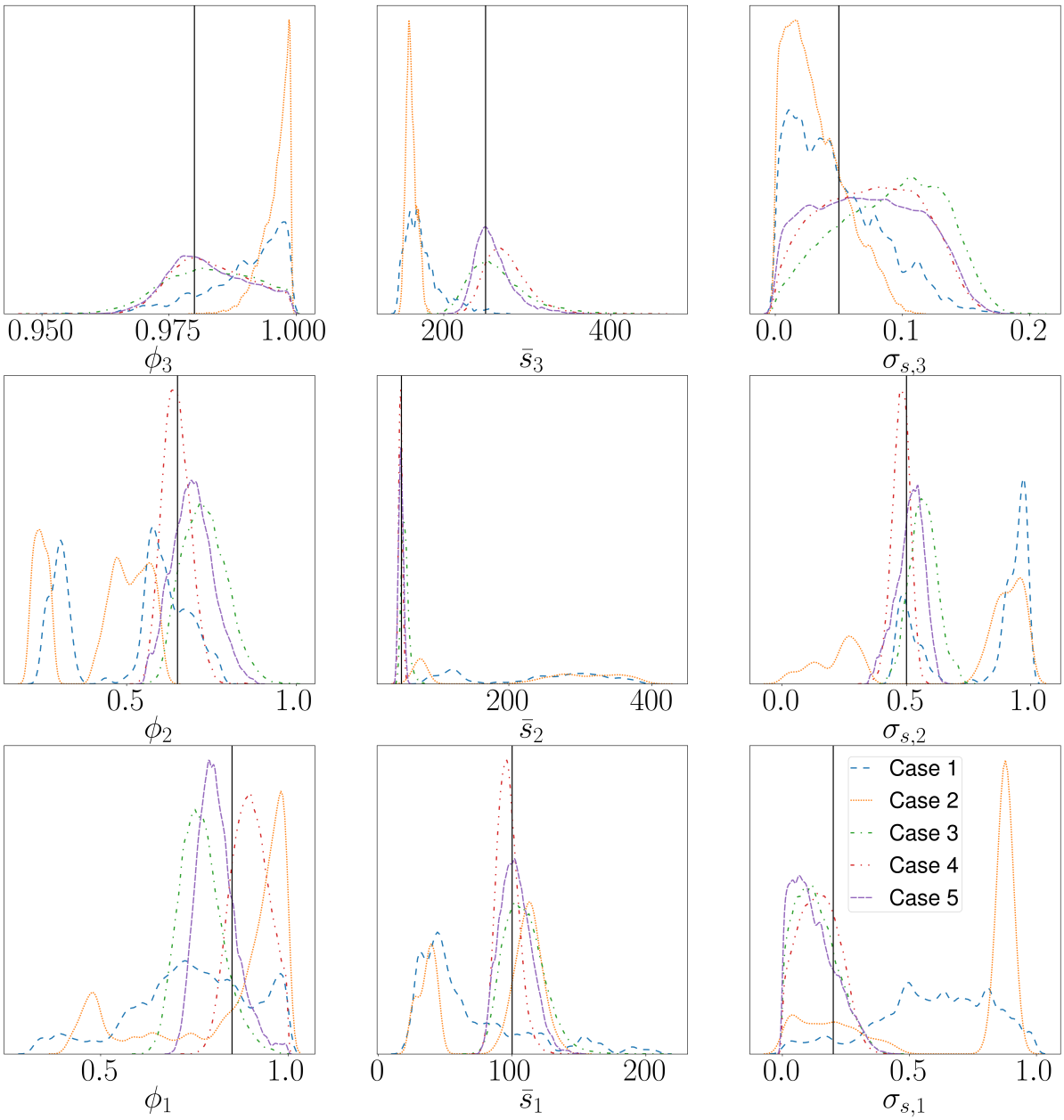

Figure 19: Posterior pdfs of the tri-layer $M_3 \circ M_2 \circ M_1$. The black vertical line corresponds to the true value. The legend refers to Table 4

For the identification of tri-layer materials, things get quite more difficult than for the previous tests. Once more, wrong identified values, very wide pdfs or bi-modal distributions can be obtained in cases 1 and 2, as expected because of the increased complexity of the problem. Even when one air-gap is considered (case 3), some pdfs are off their target values. It seems that in most cases the addition of two or three air-gaps is necessary.

In most cases, adding three air-gaps (case 5) to the observation leads to proper identifications with pdfs close to or centered on the true value. When only two air-gaps are considered (case 4), parameters can be well identified in some cases, but once again the solution suffers from the placement of a resistive layer in first or second position (see Fig. 18).

Overall, adding up to three air-gaps behind a tri-layer material makes it possible to retrieve most properties of each individual layer. By contrast, the artificial frequency-content increase of a

single observation by multiplying the number of frequencies in a signal (case 2) does not seem to significantly help the identification, if at all.

5.6 Discussion

General comments on the previous material identifications are highlighted next:

- The use of the Horoshenkov hypothesis in the JCAPL model is attractive for multi-layer identifications using impedance tubes, as an increase in the number of parameters would otherwise rapidly increase the difficulty of the inference. Since the Horoshenkov hypothesis is rooted in a statistical representation of the pore size, it is also well suited to a Bayesian inference analysis.

- Limitations of the method are related to the immediate fact that if a layer is placed behind another layer that is large or has a high resistivity, i.e., no wave is transmitted through it, then the use of one or more air-gaps would be wasted, as the observation on the microphones of the impedance tube would remain the same.

- If there is a clear rule stating how many air-gaps are necessary to identify a material having L layers, it was not elucidated in the present work. For the cases that were studied, it seems that increasing the number of air-gaps almost systematically improves the identification, and that adding even just one air-gap could drastically improve the results, going from an indeterminate state to a known state (albeit with large uncertainties, compared with cases with more observations).

- When an air-gap is added to make a new observation, an additional parameter needs to be identified (the air-gap length). It is then remarkable that despite having a higher number of parameters to identify, the cases with more air-gaps systematically improve the identification results compared with reference cases.

- Overall, it seems that all the presented numerical experiments tend to show that adding frequencies to a signal is not equivalent, and is in fact inferior, to adding observations of the same material with additional air-gaps. Although requiring additional experiments in the impedance tube, it remains a straightforward and non-intrusive method that can readily be used in most acoustic labs.

- When using a deterministic approach to inverse problems, by means of an optimization algorithm, one could directly apply this paper's method using the log-likelihood as a cost function and the log-prior as a regularization parameter.

- When using high-frequency content time-domain signals, for instance with ultrasonic transducers, the present method needs to be adapted since an impedance tube cannot be used anymore. However, one could potentially add an air-gap and a rigid plate behind the material to measure the total reflection coefficient of the combination, to cheaply obtain a second observation on the same material. This is akin to changing the angle of incidence of the ultrasonic wave, and using multiple measurements to identify material properties [26]. Adding an air-gap would also delay the arrival of the wave that was fully transmitted and then reflected on the rigid back-plate, back to the transducer, thus potentially allowing better wave decoupling in the time domain.

Additional tests were performed, where the thickness of each sample and the length of the air-gaps were fixed to their true values. This resulted in less ill-posedness for the inverse problem (i.e., less non-uniqueness and multi-modality in the pdfs). However, it was noted that the uncertainty on the inversed parameters was still greater than when air-gaps were considered, even when the thickness of the layers and the lengths of the air-gaps were still assumed unknown.

The influence of the thickness on the observed signals is correlated with that of the tortuosity α_∞ of a sample, since they both control the distance a wave travels inside the sample. In the Horoshenkov model of Eq. 8, this amounts to a potential correlation of the sample thickness with both the pore size and standard deviation of the pore sizes. These correlations are a potential source of difficulty during the inference, which highlights that constraining the sample thickness (or any other known parameter) during the identification should be done whenever possible.

In practice, one often knows the length of each stacked material. However, if the materials are truly distinct, the identification of their properties would be simpler in the first place if measurements were done individually on each layer, and there would we no need to make the inference more difficult by considering multiple layers simultaneously.

The developed method should be seen as a complement to that of Ref. [27], where the number of discrete layers in inhomogeneous materials is considered unknown (with the assumption that a discrete representation is warranted). In this case, the thickness of each layer is unknown, and becomes a parameter of the inversion procedure that cannot be discarded.

6 Conclusion

This article has introduced two potential improvements towards porous material characterization in impedance tubes.

It was first shown that using the surface impedance or reflection coefficient signals as the input of an inverse problem for the identification of the intrinsic properties of porous media would necessarily lead to biased results. This is caused by the unknown frequency dependence of the uncertainty on these signals, which are derived initially from microphone pressure measurements using a nonlinear relationship. A more efficient approach consists in directly using the pressure measurements at all the microphones for the inverse problem input, for which the error level and type are usually given by the manufacturer or known otherwise. When more than two microphones are used in the impedance tube, the approach then becomes strictly better, as more information is gained.

A numerical analysis was then conducted on 15 different materials, consisting in all the single-layer and multi-layer combinations obtained with 3 different porous materials. Using a differential evolution version of the MCMC method [52], an objective Bayesian inference strategy was followed on each material configuration to retrieve their intrinsic properties, consisting in the parameters of Horoshenkov [34] applied to the JCAPL model. The inference inputs were synthetic noisy pressure evaluated at fictive microphone positions, mimicking an experiment.

It was shown that adding an air-gap behind a material to perform one or more additional acoustic observations almost systematically led to an improved identification. In the case where multi-layers were considered (up to three), adding an air-gap allowed the disambiguation in parameter estimation that was present in the reference case without air-gap. Adding frequencies in a single observed signal was shown to be an inferior strategy when compared with adding air-gaps to increase the number of observations.

Acknowledgment

This work has been conducted under the ONERA-CNRS collaboration agreement on porous media acoustics.

Conflict of interest

The authors declare that they have no conflict of interest.

References

[1] J. M. Sabatier, H. E. Bass, L. N. Bolen, K. Attenborough, V. Sastry, The interaction of airborne sound with the porous ground: The theoretical formulation, The Journal of the Acoustical Society of America 79 (5) (1986) 1345–1352. arXiv:https://doi.org/10.1121/1.393662, doi:10.1121/1.393662.
URL https://doi.org/10.1121/1.393662

[2] M. N. Toksoz, C. H. Cheng, A. Timur, Velocities of seismic waves in porous rocks, Geophysics 41 (4) (1976) 621–645.

[3] T. Pointer, E. Liu, J. A. Hudson, Seismic wave propagation in cracked porous media, Geophysical Journal International 142 (1) (2000) 199–231. arXiv:https://academic.oup.com/gji/article-pdf/142/1/199/1603864/142-1-199.pdf, doi:10.1046/j.1365-246x.2000.00157.x.
URL https://doi.org/10.1046/j.1365-246x.2000.00157.x

[4] N. Xiang, J. M. Sabatier, Land mine detection measurements using acoustic-to-seismic coupling, in: A. C. Dubey, J. F. Harvey, J. T. Broach, R. E. Dugan (Eds.), Detection and Remediation Technologies for Mines and Minelike Targets V, Vol. 4038, International Society for Optics and Photonics, SPIE, 2000, pp. 645 – 655. doi:10.1117/12.396292.
URL https://doi.org/10.1117/12.396292

[5] J. M. Sabatier, Ning Xiang, An investigation of acoustic-to-seismic coupling to detect buried antitank landmines, IEEE Transactions on Geoscience and Remote Sensing 39 (6) (2001) 1146–1154. doi:10.1109/36.927429.

[6] A. Hosokawa, T. Otani, Ultrasonic wave propagation in bovine cancellous bone, The Journal of the Acoustical Society of America 101 (1) (1997) 558–562. doi:10.1121/1.418118.

[7] S. Chaffaı, F. Peyrin, S. Nuzzo, R. Porcher, G. Berger, P. Laugier, Ultrasonic characterization of human cancellous bone using transmission and backscatter measurements: relationships to density and microstructure, Bone 30 (1) (2002) 229–237. doi:10.1016/S8756-3282(01)00650-0.

[8] Z. E. A. Fellah, J. Y. Chapelon, S. Berger, W. Lauriks, C. Depollier, Ultrasonic wave propagation in human cancellous bone: Application of biot theory, The Journal of the Acoustical Society of America 116 (1) (2004) 61–73. doi:10.1121/1.1755239.

[9] T. Geyer, E. Sarradj, C. Fritzsche, Measurement of the noise generation at the trailing edge of porous airfoils, Experiments in fluids 48 (2) (2010) 291–308. doi:10.1007/s00348-009-0739-x.

[10] J. Schulze, J. Sesterhenn, Optimal distribution of porous media to reduce trailing edge noise, Computers & Fluids 78 (2013) 41 – 53, lES of turbulence aeroacoustics and combustion. doi:https://doi.org/10.1016/j.compfluid.2011.12.022.
URL http://www.sciencedirect.com/science/article/pii/S004579301100394X

[11] M. Mößner, R. Radespiel, Flow simulations over porous media–comparisons with experiments, Computers & Fluids 154 (2017) 358–370. doi:10.1016/j.compfluid.2017.03.002.

[12] Y.-B. Xiong, Y.-H. Zhu, P.-X. Jiang, Numerical simulation of transpiration cooling for sintered metal porous strut of the scramjet combustion chamber, Heat Transfer Engineering 35 (6-8) (2014) 721–729. arXiv:https://doi.org/10.1080/01457632.2013.837790, doi:10.1080/01457632.2013.837790.
URL https://doi.org/10.1080/01457632.2013.837790

[13] G. Huang, Z. Min, L. Yang, P.-X. Jiang, M. Chyu, Transpiration cooling for additive manufactured porous plates with partition walls, International Journal of Heat and Mass Transfer 124 (2018) 1076 – 1087. doi:https://doi.org/10.1016/j.ijheatmasstransfer.2018.03.110.
URL http://www.sciencedirect.com/science/article/pii/S0017931017355126

[14] W. Davern, Perforated facings backed with porous materials as sound absorbers-an experimental study, Applied Acoustics 10 (2) (1977) 85–112. doi:10.1016/0003-682X(77)90019-6.

[15] M. Yang, P. Sheng, Sound absorption structures: From porous media to acoustic metamaterials, Annual Review of Materials Research 47 (2017) 83–114. doi:10.1146/annurev-matsci-070616-124032.

[16] Y. Atalla, R. Panneton, Inverse acoustical characterization of open cell porous media using impedance tube measurements, Canadian Acoustics 33 (1) (2005) 11–24.

[17] Z. E. A. Fellah, S. Berger, W. Lauriks, C. Depollier, C. Aristegui, J.-Y. Chapelon, Measuring the porosity and the tortuosity of porous materials via reflected waves at oblique incidence, J. Acoust. Soc. Am. 113 (5) (2003) 2424–2433. doi:10.1121/1.1567275.

[18] Z. E. A. Fellah, F. Mitri, C. Depollier, S. Berger, W. Lauriks, J. Chapelon, Characterization of porous materials with a rigid frame via reflected waves, J. Appl. Acoust. 94 (12) (2003) 7914–7922. doi:10.1063/1.1629386.

[19] Z. E. A. Fellah, F. G. Mitri, M. Fellah, E. Ogam, C. Depollier, Ultrasonic characterization of porous absorbing materials: Inverse problem, J. Sound. Vib. 302 (4) (2007) 746–759. doi:10.1016/j.jsv.2006.12.007.

[20] J.-D. Chazot, E. Zhang, J. Antoni, Acoustical and mechanical characterization of poroelastic materials using a bayesian approach, J. Acoust. Soc. Am. 131 (6) (2012) 4584–4595. doi:10.1121/1.3699236.

[21] Z. E. A. Fellah, M. Sadouki, M. Fellah, F. Mitri, E. Ogam, C. Dépollier, Simultaneous determination of porosity, tortuosity, viscous and thermal characteristic lengths of rigid porous materials, J. App. Phys. 114 (20) (2013) 204902. doi:10.1063/1.4833546.

[22] T. Hentati, L. Bouazizi, M. Taktak, H. Trabelsi, M. Haddar, Multi-levels inverse identification of physical parameters of porous materials, J. Appl. Acoust. (2015). doi:10.1016/j.apacoust.2015.09.013.

[23] T. G. Zieliński, Normalized inverse characterization of sound absorbing rigid porous media, J. Acoust. Soc. Am. 137 (6) (2015) 3232–3243. doi:10.1121/1.4919806.

[24] K. V. Horoshenkov, A review of acoustical methods for porous material characterisation, Int. J. Acoust. Vib 22 (2017) 92–103. doi:10.20855/ijav.2017.22.1455.

[25] M. Niskanen, J.-P. Groby, A. Duclos, O. Dazel, J. Le Roux, N. Poulain, T. Huttunen, T. Lähivaara, Deterministic and statistical characterization of rigid frame porous materials from impedance tube measurements, J. Acoust. Soc. Am. 142 (4) (2017) 2407–2418. doi:10.1121/1.5008742.

[26] R. Roncen, Z. E. A. Fellah, F. Simon, E. Piot, M. Fellah, E. Ogam, C. Depollier, Bayesian inference for the ultrasonic characterization of rigid porous materials using reflected waves by the first interface, The Journal of the Acoustical Society of America 144 (1) (2018) 210–221. doi:10.1121/1.5044423.

[27] C. J. Fackler, N. Xiang, K. V. Horoshenkov, Bayesian acoustic analysis of multilayer porous media, The Journal of the Acoustical Society of America 144 (6) (2018) 3582–3592. arXiv:https://doi.org/10.1121/1.5083835, doi:10.1121/1.5083835.
URL https://doi.org/10.1121/1.5083835

[28] R. Roncen, Z. E. A. Fellah, D. Lafarge, E. Piot, F. Simon, E. Ogam, M. Fellah, C. Depollier, Acoustical modeling and bayesian inference for rigid porous media in the low-mid frequency regime, The Journal of the Acoustical Society of America 144 (6) (2018) 3084–3101. doi:10.1121/1.5080561.

[29] R. Roncen, Z. Fellah, E. Piot, E. Ogam, Bayesian inference of a human bone and biomaterials using ultrasonic transmitted signals, The Journal of the Acoustical Society of America 146 (3) (2019) 1629–1640. doi:10.1121/1.5125263.

[30] R. Roncen, Z. Fellah, E. Piot, F. Simon, E. Ogam, M. Fellah, C. Depollier, Inverse identification of a higher order viscous parameter of rigid porous media in the high frequency domain, The Journal of the Acoustical Society of America 145 (3) (2019) 1629–1639. doi:10.1121/1.5095403.

[31] M. Niskanen, O. Dazel, J.-P. Groby, A. Duclos, T. Lähivaara, Characterising poroelastic materials in the ultrasonic range-a bayesian approach, Journal of Sound and Vibration 456 (2019) 30–48. doi:10.1016/j.jsv.2019.05.026.

[32] Z. Lim, A. Putra, M. Nor, M. Yaakob, Sound absorption performance of natural kenaf fibres, Applied Acoustics 130 (2018) 107 – 114. doi:https://doi.org/10.1016/j.apacoust.2017.09.012.
URL http://www.sciencedirect.com/science/article/pii/S0003682X17305583

[33] N. Sellen, M.-A. Galland, O. Hilbrunner, Identification of the characteristic parameters of porous media using active control, in: 8th AIAA/CEAS Aeroacoustics Conference, Breckenridge, Colorado, 2002. doi:https://doi.org/10.2514/6.2002-2504.

[34] K. V. Horoshenkov, A. Hurrell, J.-P. Groby, A three-parameter analytical model for the acoustical properties of porous media, The Journal of the Acoustical Society of America 145 (4) (2019) 2512–2517. doi:10.1121/1.5098778.

[35] D. L. Johnson, J. Koplik, R. Dashen, Theory of dynamic permeability and tortuosity in fluid-saturated porous media, J. Fluid Mech. 176 (1987) 379–402. doi:10.1017/S0022112087000727.

[36] Y. Champoux, J.-F. Allard, Dynamic tortuosity and bulk modulus in air-saturated porous media, J. Appl. Acoust. 70 (4) (1991) 1975–1979. doi:10.1063/1.349482.

[37] S. R. Pride, F. D. Morgan, A. F. Gangi, Drag forces of porous-medium acoustics, Phys. Rev. B 47 (9) (1993) 4964–4978. doi:10.1103/PhysRevB.47.4964.

[38] D. Lafarge, P. Lemarinier, J. F. Allard, V. Tarnow, Dynamic compressibility of air in porous structures at audible frequencies, J. Acoust. Soc. Am. 102 (4) (1997) 1995–2006. doi:10.1121/1.419690.

[39] K. V. Horoshenkov, A. Hurrell, J.-P. Groby, Erratum: A three-parameter analytical model for the acoustical properties of porous media [j. acoust. soc. am. 145 (4), 2512–2517 (2019)], The Journal of the Acoustical Society of America 147 (1) (2020) 146–146. doi:10.1121/10.0000560.

[40] R. Roncen, Z. E. A. Fellah, E. Ogam, Bayesian inference of human bone sample properties using ultrasonic reflected signals, The Journal of the Acoustical Society of America 148 (6) (2020) 3797–3808. doi:10.1121/10.0002878.

[41] J. Allard, N. Atalla, Propagation of Sound in Porous Media: Modelling Sound Absorbing Materials 2e, John Wiley & Sons, New York, 2009. doi:10.1002/9780470747339.

[42] O. Dazel, J.-P. Groby, B. Brouard, C. Potel, A stable method to model the acoustic response of multilayered structures, Journal of Applied Physics 113 (8) (2013) 083506. doi:10.1063/1.4790629.

[43] M. Åbom, H. Bodén, Error analysis of two-microphone measurements in ducts with flow, The journal of the acoustical society of America 83 (6) (1988) 2429–2438. doi:10.1121/1.396322.

[44] R. C. Smith, Uncertainty quantification: theory, implementation, and applications, Vol. 12, Siam, Philadelphia, 2013.

[45] N. Xiang, C. Fackler, Objective bayesian analysis in acoustics, Acoust. Today 11 (2) (2015) 54–61.

[46] C. Brunetti, Bayesian model selection in hydrogeophysics and hydrogeology, Ph.D. thesis, Université de Lausanne, Faculté des géosciences et de l'environnement (2018).

[47] N. Metropolis, A. W. Rosenbluth, M. N. Rosenbluth, A. H. Teller, E. Teller, Equation of state calculations by fast computing machines, The journal of chemical physics 21 (6) (1953) 1087–1092. doi:10.1063/1.1699114.

[48] W. K. Hastings, Monte carlo sampling methods using markov chains and their applications, Biometrika 57 (1) (1970) 97–109. doi:10.1093/biomet/57.1.97.

[49] R. Storn, K. Price, Differential evolution–a simple and efficient heuristic for global optimization over continuous spaces, J. Global Optim. 11 (4) (1997) 341–359. doi:10.1023/A:1008202821328.

[50] C. J. ter Braak, J. A. Vrugt, Differential evolution markov chain with snooker updater and fewer chains, Statistics and Computing 18 (4) (2008) 435–446. doi:10.1007/s11222-008-9104-9.

[51] J. A. Vrugt, C. Ter Braak, C. Diks, B. A. Robinson, J. M. Hyman, D. Higdon, Accelerating markov chain monte carlo simulation by differential evolution with self-adaptive randomized subspace sampling, International Journal of Nonlinear Sciences and Numerical Simulation 10 (3) (2009) 273–290.
URL https://www.osti.gov/biblio/960766

[52] E. Laloy, J. A. Vrugt, High-dimensional posterior exploration of hydrologic models using multiple-try dream(zs) and high-performance computing, Water Resour. Res. 48 (1) (2012) n/a–n/a, w01526. doi:10.1029/2011WR010608.

[53] A. Gelman, D. B. Rubin, Inference from iterative simulation using multiple sequences, Statistical science 7 (4) (1992) 457–472. doi:10.1214/ss/1177011136.

[54] E. M. Shockley, J. A. Vrugt, C. F. Lopez, PyDREAM: high-dimensional parameter inference for biological models in python, Bioinformatics 34 (4) (2017) 695–697. arXiv:https://academic.oup.com/bioinformatics/article-pdf/34/4/695/25117213/btx626.pdf, doi:10.1093/bioinformatics/btx626.
URL https://doi.org/10.1093/bioinformatics/btx626

[55] A. Wirgin, The inverse crime, arXiv preprint math-ph/0401050 (2004).

[56] M. Waskom, O. Botvinnik, D. O'Kane, P. Hobson, S. Lukauskas, D. C. Gemperline, T. Augspurger, Y. Halchenko, J. B. Cole, J. Warmenhoven, J. de Ruiter, C. Pye, S. Hoyer, J. Vanderplas, S. Villalba, G. Kunter, E. Quintero, P. Bachant, M. Martin, K. Meyer, A. Miles, Y. Ram, T. Yarkoni, M. L. Williams, C. Evans, C. Fitzgerald, Brian, C. Fonnesbeck, A. Lee, A. Qalieh, mwaskom/seaborn: v0.8.1 (september 2017) (Sep. 2017). doi:10.5281/zenodo.883859.
URL https://doi.org/10.5281/zenodo.883859